Increased performance improvement of lithium-ion batteries by dry powder coating of high-nickel NMC with nanostructured fumed ternary lithium metal oxides

Increased Performance Improvement of Lithium Ion Batteries by Dry Powder Coating of High-Nickel NMC with Nanostructured Fumed Ternary Lithium Metal Oxides

Marcel J. Herzog, Nicolas Gauquelin, Daniel Esken, Johan Verbeeck, Jürgen Janek*

M. J. Herzog, Prof. J. Janek,
Institute of Physical Chemistry & Center for Materials Research Justus-Liebig-University
Giessen, Heinrich-Buff-Ring 17, 35392 Giessen, Germany
E-mail: Juergen.Janek@phys.Chemie.uni-giessen.de

Dr. N. Gauquelin, Prof. J. Verbeeck
Electron Microscopy for Materials Science, University of Antwerp, Campus Groenenborger,
Groenenborgerlaan 171, 2020 Antwerpen, Belgium and NANOlab Center of Excellence, University
of Antwerp, Antwerp, Belgium

M. J. Herzog, Dr. D. Esken
Evonik Operations GmbH, Rodenbacher Chaussee 4, 63457 Hanau-Wolfgang, Germany

Abstract

Dry powder coating is an effective approach to protect the surfaces of layered cathode active materials (CAMs) in lithium ion batteries. Previous investigations indicate an incorporation of lithium ions in fumed Al_2O_3, ZrO_2 and TiO_2 coatings on $LiNi_{0.7}Mn_{0.15}Co_{0.15}O_2$ during cycling, improving the cycling performance. Here, this coating approach is transferred for the first time to fumed ternary $LiAlO_2$, $Li_4Zr_3O_8$ and $Li_4Ti_5O_{12}$ and directly compared with their lithium-free equivalents. All materials could be processed equally and their nanostructured small aggregates accumulate on the CAM surfaces to quite homogeneous coating layers with a certain porosity. The NMCs coated with lithium-containing materials show an enhanced improvement in overall capacity, capacity retention, rate performance and polarization behavior during cycling, compared to their lithium-free analogues. The highest rate performance was achieved with the fumed ZrO_2-coating, while the best long-term cycling stability with the highest absolute capacity was obtained for fumed $LiAlO_2$ coated NMC. The optimal coating agent for NMC to achieve a balanced system is fumed $Li_4Ti_5O_{12}$, providing a good compromise between high rate capability and good capacity retention. The coating agents prevent CAM particle cracking and degradation in the order $LiAlO_2$ $\approx$ Al_2O_3 > $Li_4Ti_5O_{12}$ > $Li_4Zr_3O_8$ > ZrO_2 > TiO_2. A schematic model for the protection and electrochemical performance enhancement of high-nickel NMC with fumed metal oxide coatings is sketched. It becomes apparent that physical and chemical characteristics of the coating significantly influence the performance of NMC. A high degree of coating layer porosity is favorable for the rate capability, while a high coverage of the surface, especially in vulnerable grain

boundaries, is enhancing the long-term cycling stability and improving the cracking behavior of NMC. While zirconium-containing coatings can be ascribed the best chemical properties for high rate performances, aluminum-containing coatings are attributed a superior chemical nature to protect high-nickel NMC.

Keywords: dry coating, capacity fading, fumed metal oxide, nanostructured oxide, cathode modification, cathode active material, lithium ion battery

1. Introduction

Layered NMC ($LiNi_xMn_yCo_zO_2$ with $x + y + z = 1$) is one of the most promising candidates for cathode active materials (CAMs) to meet the rising demands for high-performance lithium ion batteries. The content of the respective metal ions can be varied, whereby a higher nickel content enhances the specific capacity by allowing increased degrees of delithiation; a higher manganese fraction stabilizes the α-$NaFeO_2$-type crystal structure and a higher cobalt content improves the reversibility by reducing the cation mixing of nickel into the lithium layers.[1,2] Compared to cobalt-rich materials, a high-nickel content also leads to relatively lower costs.[2,3] This makes high-nickel NMC ($LiNi_xMn_yCo_zO_2$, $x + y + z = 1$, $x > 0.5$) especially interesting. However, an increased nickel content leads to an increased reactivity of the CAM surface, resulting in a decreased capacity retention and cycle life.[4] By direct contact with the reactive surface, the electrolyte starts to decompose during cycling, resulting in deposition of decomposition products at the cathode electrolyte interface, which leads to increased resistance.[3,4]

Additionally, surface transformations like the formation of a spinel and/or rock salt phase due to transition metal rearrangement, the reduction of Ni^{4+} in a highly delithiated state and oxygen loss destabilize the material.[5,6,7] These phase transitions combined with the volume change during (de)lithiation initiate cracks in the CAM particles, leading to subsequent particle decay.[8,9] A general problem with the conducting salt $LiPF_6$, most commonly used in liquid electrolytes for LIBs, is its reaction with trace amounts of H_2O, which are present in all commercial cell constituents, and the resulting generation of HF.[10] The corrosive HF dissolves transition metal ions out of the CAM surface, which causes lattice distortion.[11] These degradation mechanisms are a severe drawback, which still has to be solved for a commercialization of high-nickel CAMs.

Surface coating is a simple as well as effective method to mitigate these aging problems during cycling. The primary function of the coating layer is to suppress the direct contact between the CAMs´ surfaces and the liquid electrolyte.[12] The most commonly used materials for coating of CAM surfaces are a variety of nominally lithium-free binary metal oxides, e.g. SiO_2[13], CeO_2[14], Al_2O_3[15], TiO_2[16], ZrO_2[17], etc. Because these metal oxide coating materials often exhibit a rather poor lithium ion conductivity, inorganic materials containing lithium ions are recently recommended more and more in the literature.[18-20] For example, Liu et al.[21] coated Al_2O_3 and $LiAlO_2$ on NMC 622 ($LiNi_{0.6}Mn_{0.2}Co_{0.2}O_2$) and analyzed the influence on cycling performance. In comparison, for the $LiAlO_2$-coated sample, a superior capacity and rate capability was observed.

In comparison to wet-chemical-[14], sol-gel-[15] and ALD-coating[22], the dry coating approach is an easy to apply, cost effective and environmental friendly method to form surface coatings on CAMs.[23,24] In two previous reports, we described the dry coating process of high-nickel NMC with fumed Al_2O_3, TiO_2 and ZrO_2, using a high-energy mixer.[23,24] In this process, the micron sized CAM particles act as core particles and are coated directly by mechanical forces with the coating agent (submicron-sized particles), without using any solvents and binders. Fumed metal oxides have proven to be particularly suitable for this procedure, because of their small and characteristic nanostructured aggregates with a certain degree of branching.[23,24] The resulting partly porous coating layer adheres at the surface of the CAM without an additional sintering step. We assume that the channels in the coating can be penetrated by the liquid electrolyte, contributing to lithium ion diffusion to and from the NMC surface. The coated NMC materials show a significantly improved rate performance compared to uncoated NMC.[23,24]

In-depth investigations revealed that lithium ions are incorporated to a certain degree in fumed Al_2O_3, TiO_2 and ZrO_2 coating layers on high-nickel NMC during cycling.[23,24] These lithium-doped metal oxides provide an increased lithium ion conductivity, contributing to the enhanced rate performance of the coated CAMs. We expect lithium ions to diffuse through the coating following preferential pathways with the largest local diffusion coefficients. In areas, where no electrolyte filled pores are available, the lithium ions need to migrate across the coating material, and lithium ions seem to be incorporated in the coating. Along this defined path, the lithium ion diffusion coefficient is enhanced permanently and thus also the rate performance.[24] Therefore, besides the porosity of the coating layer, the lithium ion diffusion coefficient of the coating material is also an important factor for the rate performance.[23]

In this article, we investigate whether the cycling performance of CAMs can be further enhanced by using ternary lithium-containing nanostructured fumed coating agents. For this purpose, fumed lithium aluminate, lithium titanate, lithium zirconate, and the corresponding lithium-free fumed binary metal oxides are coated on high-nickel NMC. The characteristics of the coated materials and their electrochemical performance are evaluated in detail. The results reveal an improved enhancement in overall capacity, rate capability, long-term cycling stability and polarization behavior for NMCs coated with the respective ternary lithium metal oxides, as long as the coating layer porosity is not severely reduced. The coating layer porosity is an important physical parameter influencing the cycling performance.

2. Results and Discussion

2.1 Coating Materials and Coating Process

Nanostructured fumed metal oxides were found to be especially suitable as coating agents for dry powder coating of CAMs.[23,24] These materials are produced by flame hydrolysis, wherein nuclei are generated in the flame, with growth processes following, mostly resulting in primary particles with a size of about 10 to 15 nm. The primary particles are chemically bonded to each other to build

highly nanostructured three-dimensional formations with some degree of branching, the so-called aggregates.[25] These aggregates cannot be easily separated into discrete primary particles anymore and accumulate to agglomerates.[25] For fumed metal oxides, very high BET surfaces are characteristic.[25] Figure 1 shows scanning electron microscopy (SEM) images of discrete aggregates of the fumed metal oxides used. The corresponding BET surface areas are shown in Table 1.

The major aim of this work was to investigate the effect of the chemical composition of the coating material on the cycling performance. Physical parameters, like the porosity of the coating layer and the surface coverage of the CAM, have also a significant impact on the cycling performance and are mainly influenced by the BET surface and consequently the primary particle size of the coating material.[23] In order to minimize the influence of these physical parameters, coating agents with almost similar BET characteristics were selected.
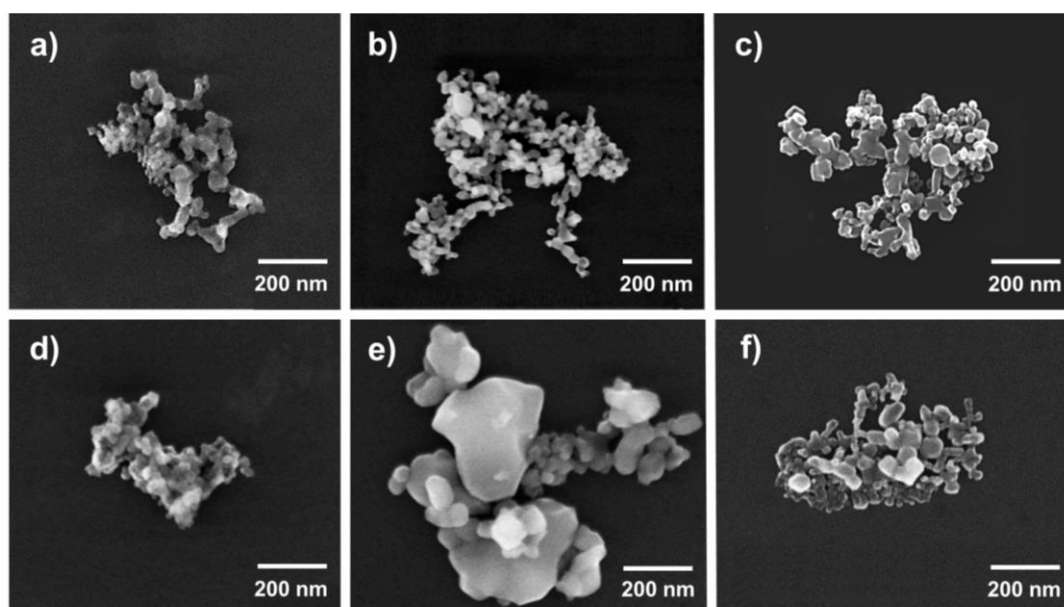

Figure 1. *SEM images of discrete aggregates of the fumed metal oxides used (a: Al_2O_3, b: ZrO_2, c: TiO_2, d: $LiAlO_2$, e: $Li_4Zr_3O_8$, f: $Li_4Ti_5O_{12}$).*

Another special feature of the applied fumed materials is that all of them show a crystalline structure. While Al_2O_3 shows the γ-Al_2O_3 structure[25], the fumed ZrO_2 phase is mostly tetragonal, the TiO_2 material consists of a mixture of anatase and rutile[25], $LiAlO_2$ shows the α-phase, $Li_4Zr_3O_8$ is tetragonal and $Li_4Ti_5O_{12}$ is cubic. The respective results on the crystallographic characterization of the coating materials, which are not reported in literature so far, are shown in Figure S1.

For dry powder coating, the CAM and coating material powders are mixed in a high-energy mixer without any solvent or binder. The nanostructured fumed metal oxides are de-agglomerated to smaller aggregates by the high shear forces and start to interact with the surface of the CAM particles. The de-agglomeration of the fumed metal oxides is crucial for our dry coating method.

The tiny nanostructured aggregate dimension ensures a good adherence of the coating material to the CAM particle surfaces. The formed coating layer is composed of three-dimensional nanostructured aggregates with different sizes and degrees of branching, which are interlocked and compressed to a certain degree at the CAM surface. An additional sintering step at high temperatures after dry coating is not needed to fix the coating material on the CAM surface. For more details about the dry powder coating process principle, we refer to a previous report.[24]

2.2 Analysis of Coated Cathode Active Materials

2.2.1 Influence of Coating Process on Host Cathode Active Material

The X-ray powder diffraction (XRD) peaks of NMC coated with 1 wt-% of the respective coating agent and uncoated NMC are presented in supplementary Figure S2. All diffraction reflexes are indexed based on the α-NaFeO$_2$ structure with the R-3m space group. There was no difference observed in the XRD patterns of the coated and the uncoated NMCs, confirming that the coating process does not have any influence on the bulk crystal structure of the host CAM. Additionally, no extra diffraction signals of the thin coating layer were observed, which is expected in view of the small mass fractions of the coating materials.

2.2.2 Characterization of the Coating Layers

After the dry coating process, the coated NMCs are analyzed by scanning electron microscopy combined with energy dispersive X-ray spectroscopy (SEM-EDX). In the elemental mappings of all coated NMCs, an almost continuous and homogeneous coverage of all CAM particles can be seen, as indicated by the signal of the respective metals of the coating materials (Figure 2). No significant amount of large coating agglomerates was found, revealing that de-agglomeration of nanostructured fumed ternary lithium metal oxides is as successful as for the binary lithium-free metal oxides. Additionally, no unattached agglomerates or aggregates of coating material are found, indicating strong adhesion of all coating materials to the substrate. Consequently, the lithium metal oxide coating agents can be processed equally in the dry powder coating approach to the corresponding binary metal oxides. We already demonstrated in a previous article[24] that the NMC host material withstands the strong shear forces in the high-energy mixing process.

Figure 3 presents SEM images of NMC coated with the respective lithium-containing and -free metal oxides, compared to uncoated NMC. The NMC material itself consists of small primary NMC single crystals, which are assembled to form the secondary particle structure. The surface of secondary particles is very rough, clearly showing the primary particles. The coating material can be distinctly seen at the surface of all coated NMCs in the SEM images, revealing how the coating material is distributed. For all coating materials a quite continuous coating layer is achieved. In contrast, the pristine NMC shows smooth and clean surfaces of the primary NMC crystallites.

The BET surface areas of the coating materials (see Table 1) are quite well reflected in the surface coverage of the CAM after coating. Relatively close BET surface areas result in quite similar surface coverages of the CAM. Fumed Al$_2$O$_3$ and LiAlO$_2$ coating materials show slightly higher BET surface areas, resulting in slightly higher surface coverages of NMC as observed for ZrO$_2$, TiO$_2$ and Li$_4$Ti$_5$O$_{12}$ coating agents. The only exception here is Li$_4$Zr$_3$O$_8$, which has a significant lower BET surface area. Despite of the low BET surface area and the coarse particles (see Figure 1), the Li$_4$Zr$_3$O$_8$ particles result in a relatively high coverage of the NMC surface. The coarse Li$_4$Zr$_3$O$_8$ particles appear to cover predominantly surface depressions and grain boundaries and form a dense, non-porous coating in these areas, whereas the protruding NMC crystallites are mostly uncovered.

It is conspicuous that the $Li_4Ti_5O_{12}$ coating also contains, besides fine particles, a fraction of coarser dense particles located predominantly in surface depressions and grain boundaries, as observed for $Li_4Zr_3O_8$, although it shows a BET surface area in the same range than TiO_2. The influence of the respective coating layers on the cycling performance is evaluated in the electrochemical evaluation part below.
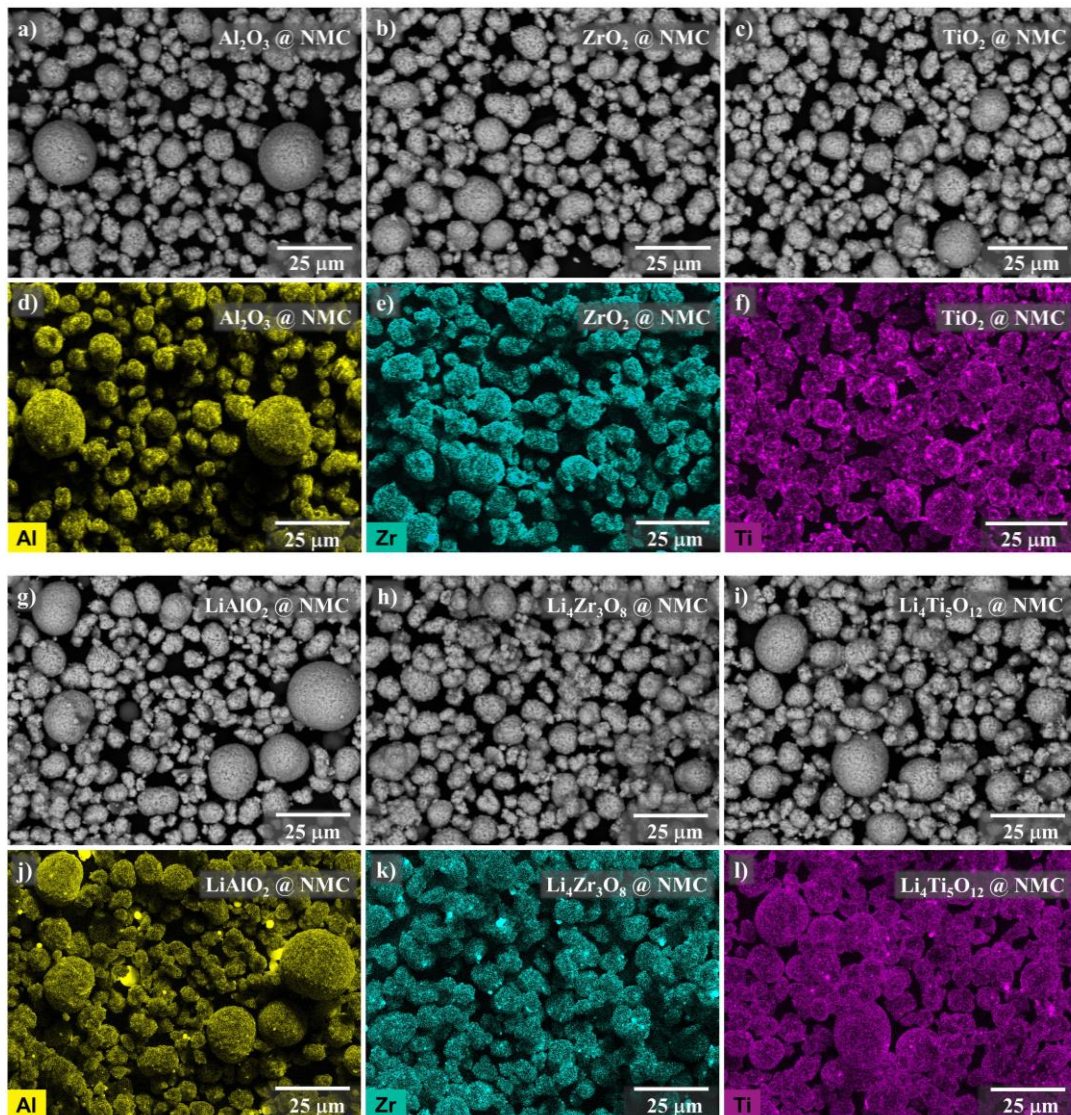

Figure 2. SEM images of NMC701515 coated with the respective coating phase (a, b, c, g, h, i: Backscattered electrons (BSE) image; d, e, f, j, k, l: EDX mapping of the respective metal of the coating agent).
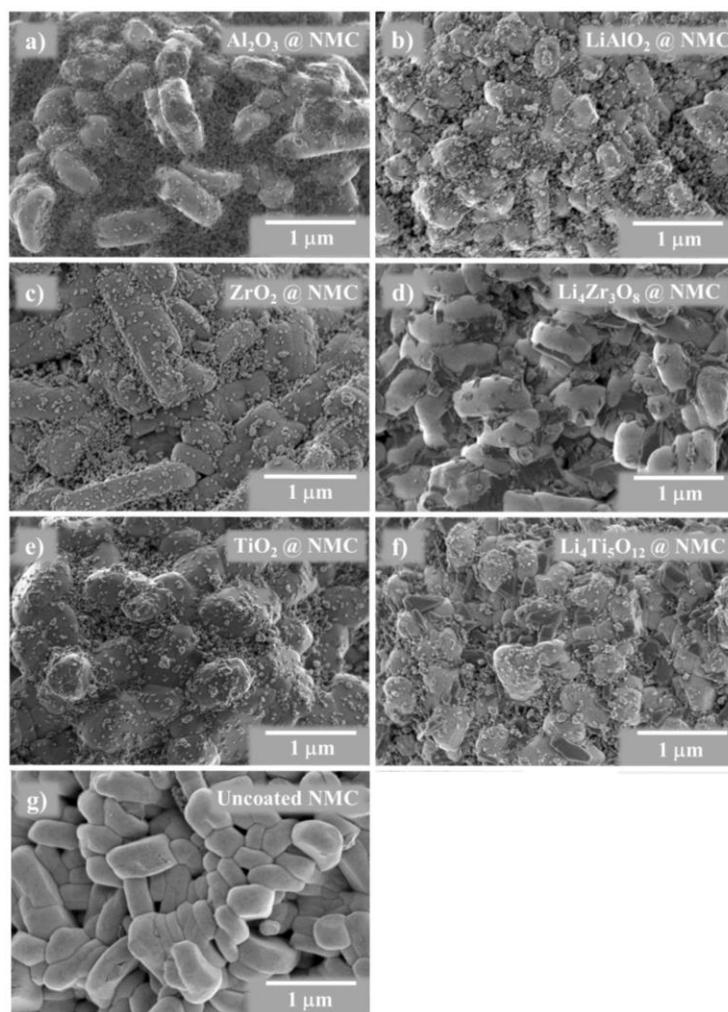
Figure 3. *SEM images of NMC701515 coated with 1 wt-% of the respective coating material (a: Al$_2$O$_3$, b: LiAlO$_2$, c: ZrO$_2$, d: Li$_4$Zr$_3$O$_8$, e: TiO$_2$, f: Li$_4$Ti$_5$O$_{12}$) and uncoated NMC (g).*

Table 1: *BET surface areas of the respective fumed metal oxides and NMC dry coated by them.*

		Al$_2$O$_3$	LiAlO$_2$	ZrO$_2$	Li$_4$Zr$_3$O$_8$	TiO$_2$	Li$_4$Ti$_5$O$_{12}$
BET surface (m^2/g)		65	61	45	13	50	47

	uncoated NMC	Al$_2$O$_3$ @ NMC	LiAlO$_2$ @ NMC	ZrO$_2$ @ NMC	Li$_4$Zr$_3$O$_8$ @ NMC	TiO$_2$ @ NMC	Li$_4$Ti$_5$O$_{12}$ @ NMC
BET surface (m^2/g)	0.5	1.0	1.0	0.9	0.6	0.9	1.0

Scanning transmission electron microscopy (STEM) analyses of cross-sections of NMC coated with 1 wt-% of the respective coating agent reveal in more detail how the coating layer is composed (Figure S3). The coating consists of small accumulated aggregates, which are densified on the
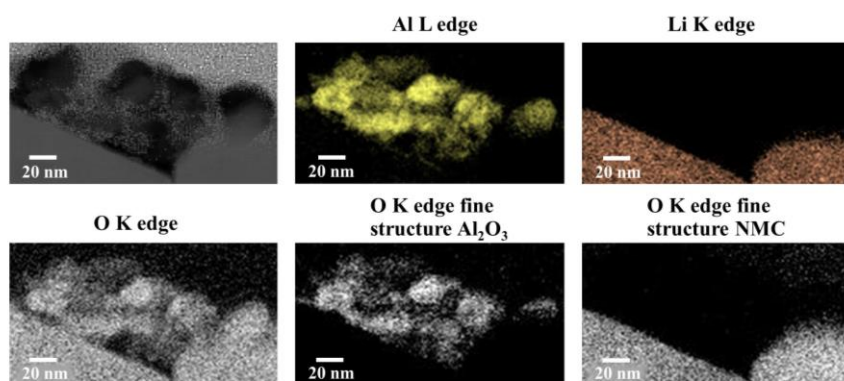
surface to a certain extent. The particles are not forming a completely dense layer, like in common types of coating approaches. The coating layers achieved by dry powder mixing, using fumed metal oxides, still show some channels and voids and are partly porous. We expect that these pores can be penetrated by liquid electrolyte, enhancing the rate performance.[23,24]

The porosity of the coating layers is also proven by BET surface area measurements of the coated NMCs (see Table 1). All coated CAMs show BET surface areas in the same range (~1.0 m^2 g^{-1}), which is almost double of the value for uncoated NMC (~0.5 m^2 g^{-1}). Only $Li_4Zr_3O_8$ coated NMC shows a lower BET surface area, because of the low surface area of the coating material itself. A clear difference in coating material particle size can only be observed for $Li_4Zr_3O_8$, showing significantly larger particles than the other materials (Figure S3d).
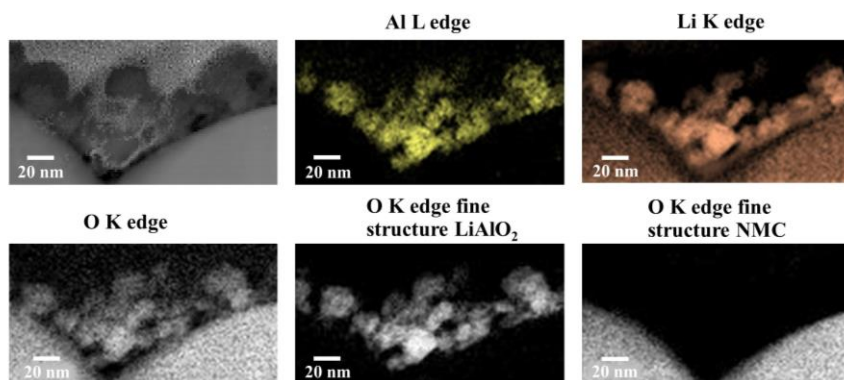
The thickness of the coatings highly depends on the morphology of the surface of the host material. The roughness of the NMC surface is smoothened by the fumed metal oxide coating layer. In areas of surface cavities, the local coating thickness is raised, whereas the protruding sites are only thinly covered. For this reason, a reasonable value for the coating thickness cannot be assigned. This is also the reason for the difference in the coating layer thicknesses of the different coating materials in the regions analyzed by STEM, shown in Figure S3. Coating layer thicknesses from 15 to 150 nm were observed.

Figure S4 displays the electron energy-loss near edge structure (ELNES) spectra of the low loss regions (where the Li K edge can be seen for the Li containing materials) and O K-edges of the respective coating materials before coating and after coating on high-nickel NMC as well as the transition metal $L_{2,3}$ edges, confirming that the chemical composition of the coating materials is not affected by the high-intensity dry coating process. For Zr-containing materials, the Zr $L_{2,3}$ fine structure is not reported as it does not give any additional phase information. The phases of the different coatings can be confirmed using these fine structures as anatase for TiO_2[26], and γ-Al_2O_3[24,27] for the non-lithiated compounds. The exact symmetry of the fumed ZrO_2 cannot be inferred directly from electron energy loss spectroscopy (EELS) data but is a mixture of monoclinic and tetragonal ZrO_2 according to XRD (Figure S1). The lithium- and titanium-containing coating agent is identified as spinel $Li_4Ti_5O_{12}$[28,29]. For $LiAlO_2$ the phase was confirmed using its band gap as α-$LiAlO_2$[30] as the band gap was measured around 6 eV (see Figure S4). For $Li_4Zr_3O_8$, the edge has yet not been reported and we can only conclude that the compound contains lithium and that it is the same as the reference coating identified by XRD as $Li_4Zr_3O_8$ (Figure S1).

a) Al₂O₃ @ NMC

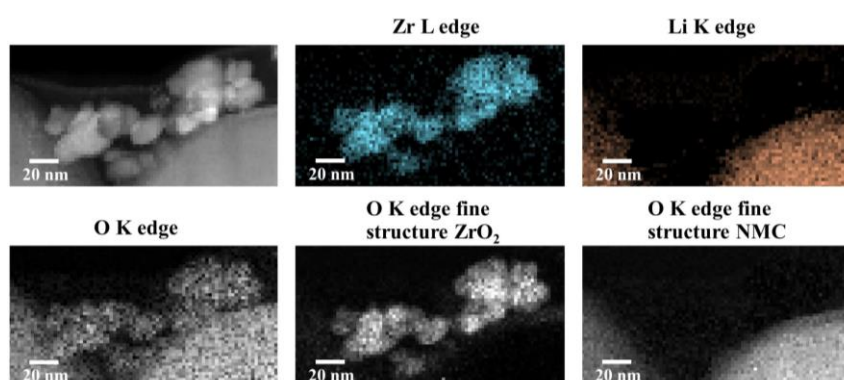Al L edge

Li K edge

O K edge

O K edge fine structure Al₂O₃

O K edge fine structure NMC

b) LiAlO₂ @ NMC

Al L edge

Li K edge

O K edge

O K edge fine structure LiAlO₂

O K edge fine structure NMC

c) ZrO₂ @ NMC

Zr L edge

Li K edge

O K edge

O K edge fine structure ZrO₂

O K edge fine structure NMC

d) Li₄Zr₃O₈ @ NMC

Zr L edge

Li K edge

O K edge

O K edge fine structure Li₄Zr₃O₈

O K edge fine structure NMC
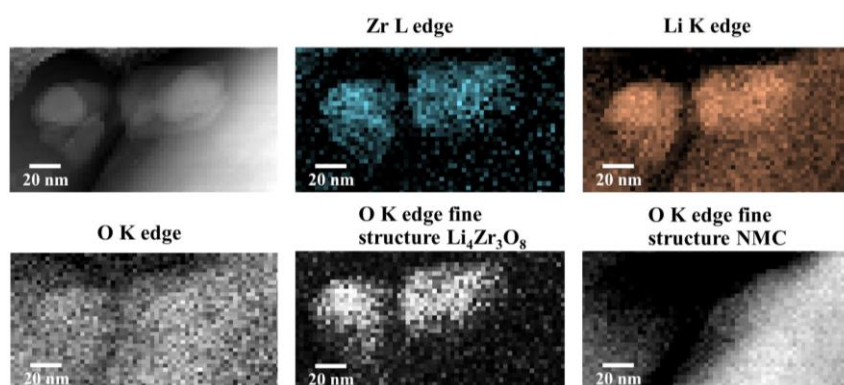
Figure 4. Continued.
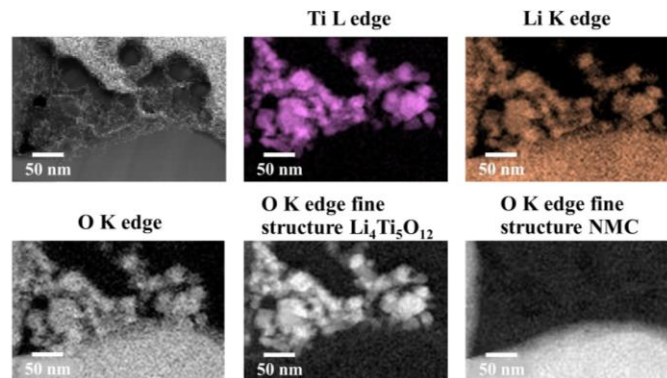
e) TiO₂ @ NMC
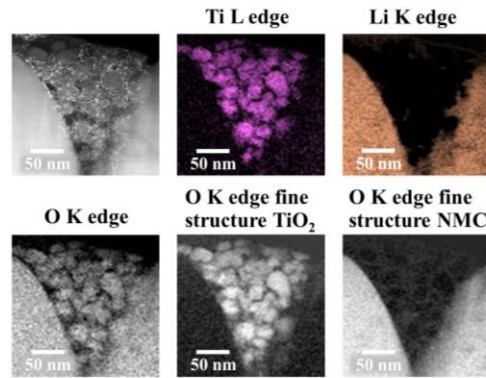
f) Li₄Ti₅O₁₂ @ NMC

Figure 4. *STEM-EELS analysis and spectra of cross-sections of NMC701515 coated with 1 wt-% of the respective coating material. Compositional spectrum images corresponding to the Al L₂,₃-edge/Zr L₂,₃/Ti L₂,₃ edge, Li and O K-edges are respectively shown (a: Al₂O₃, b: LiAlO₂, c: ZrO₂, d: Li₄Zr₃O₈, e: TiO₂, f: Li₄Ti₅O₁₂ coated NMC). The signals of the O K-edge regions are separated by MLLS fitting using fine structures corresponding to the respective coating material and to NMC701515.*

Figure 4 shows EELS maps of the coated NMC materials. The coating layers are clearly visible on top of the cathode material in the mappings of the respective coating metals. Mappings of the Li K-edges confirm the presence of lithium in the coating layers, consisting of the ternary lithium metal oxides. In contrast, in the mappings of the NMCs coated with the lithium-free coating agents, lithium is only detected in the NMC material. O K-edge mappings show the presence of oxygen in the NMC and the coating materials. Multi-linear least squares (MLLS) fitting of the O K-edge signals with experimental spectra of the O K-edge of the individual coating materials and the NMC701515 confirms the respective identities of the coating materials and their presence only on top of the NMC surface.
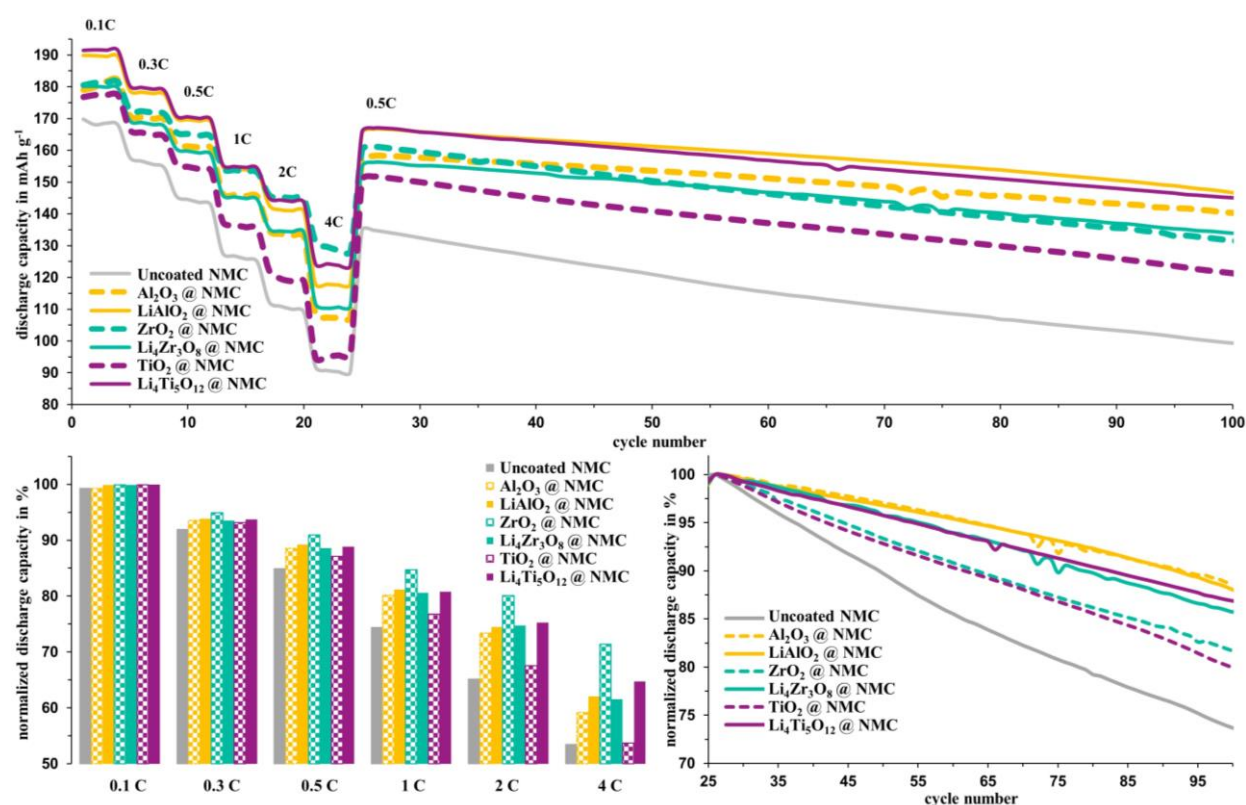
2.3 Electrochemical Characterization

Figure 5. *Cycling performance of NMC701515 dry-powder-coated with the respective fumed metal oxides (1 wt-%) compared to uncoated NMC at room temperature (average of 3 cells each). Top: Absolute discharge capacities; Bottom: Normalized discharge capacities in % (left: rate test, right: long-term cycling sequence).*

To investigate the influence of the individual coating materials on the cycling performance of high-nickel NMC, the samples with the respective coatings (fraction of 1 wt-% each) are tested in coin half-cells (with lithium metal anode). The cycling performances of the coated materials are compared against each other and uncoated NMC701515 as reference in Figure 5.

All fumed metal oxide coatings undoubted enhance the electrochemical performance of high-nickel NMC. Plotting the absolute discharge capacities (Figure 5, top) reveals that all coatings enable a higher initial specific discharge capacity, compared to bare NMC. This effect is ascribed to a beneficial secondary effect of the coating layers, ameliorating the storage properties of high-nickel NMC by reducing direct contact with CO_2 and H_2O from air (for a detailed explanation we refer to our previous report[23]). The reactive surfaces of high-nickel materials suffer under lithium loss due to the formation of surface impurities, mostly carbonates and hydroxides, leading to a capacity decrease.[31,32] It is obvious, that all NMCs coated with lithium metal oxides (except of $Li_4Zr_3O_8$, probably due to inferior physical properties of the coating, i.e. a lithium ion blocking effect caused by the dense coarse coating particles (see Figure S3) and the lower porosity of the coating layer) show a higher absolute overall capacity than those with lithium-free oxides. This may probably be due to the additional lithium ions that have been brought into the system. The enhanced overall capacity is a major advantage of using ternary lithium metal oxide coating agents.

In the first part of the cycling sequence, the cells are discharged at varying rates from 0.1C to 4C to evaluate the materials' rate capabilities. The discharge curves of the individual current densities are shown in Figure S5. The discharge capacities of the electrodes progressively drop for all samples with increasing C-rates, resulting from limited lithium ion or electron transport in the electrodes.[33] For all coated NMCs, a superior rate performance compared to uncoated NMC is found. Even though all coated CAMs, except of $Li_4Zr_3O_8$ coated NMC, have a similar BET surface area (see Table 1) and consequently similar porosities of the coating layers (physical parameter), the rate capabilities vary significantly. This can be attributed to different lithium ion diffusivities in the varying chemical compositions of the coatings. To enable a better comparison of the influence of the individual coating materials on the rate performance of high-nickel NMC, the discharge capacity is normalized and the rate test sequence is plotted in a column plot (Figure 5; bottom, left).

The highest rate performance is obtained with ZrO_2-coated NMC, showing a normalized discharge capacity of 71% at a rate of 4C, followed by $Li_4Ti_5O_{12}$ (65% at 4C), $LiAlO_2$ (62% at 4C), $Li_4Zr_3O_8$ (61% at 4C), Al_2O_3 (59%) and TiO_2 coated NMC (54% at 4C). In comparison, the uncoated NMC shows with 53% of normalized discharge capacity at a rate of 4C the lowest rate performance. These results indicate a higher lithium ion resistance of the solid electrolyte interface (SEI) formed by electrolyte decomposition species on the uncoated CAM surface than that of the partly porous coating layers. We conclude that the coating layers successfully prevent decomposition of electrolyte on the reactive surface of high-nickel NMC and growth of a thick SEI layer.

In general, an improvement in rate performance is observed by applying lithium metal oxide coating materials, compared to their lithium-free equivalents. The only exception here is $Li_4Zr_3O_8$, showing an inferior rate performance. By using $LiAlO_2$ instead of Al_2O_3, the normalized rate performance could be improved by ~5% at a rate of 4C. This rather small improvement suggests that lithium may already be incorporated into the Al_2O_3 coating during cycling. Using $Li_4Zr_3O_8$ instead of ZrO_2 results in a decreased rate performance by ~14% at a rate of 4C. The reason is probably, as explained before, the lower porosity of the $Li_4Zr_3O_8$ coating layer. The fact that the highest rate performance among all combinations is observed for ZrO_2 coated NMC indicates a high lithium ion diffusivity within the ZrO_2 coating during cycling. While the ZrO_2 coated sample is showing a slightly lower BET surface area (worse physical properties, see Table 1) than $LiAlO_2$ and $Li_4Ti_5O_{12}$ coated NMC, it still shows the highest absolute discharge capacity at a rate of 4C. Although the $Li_4Zr_3O_8$ coating layer has a lower porosity, the rate performance is in a similar range to that of the NMC coated by $LiAlO_2$ and $Li_4Ti_5O_{12}$. This points to good chemical properties (lithium ion diffusivities in the coating material) of the zirconium-containing coating agents. It can be expected, that by using the ternary lithium metal oxide ($Li_4Zr_3O_8$) instead of ZrO_2, the rate performance can be enhanced, like it was observed for the aluminum- and titanium-containing materials, when the physical parameters of the coating layer can be maintained. This is subject of further research. Compared to TiO_2 coated NMC, the normalized rate performance is increased by 21% at a discharge rate of 4C when $Li_4Ti_5O_{12}$ is used as coating material. This strong enhancement in rate capability reveals that the species formed of fumed TiO_2 by lithium incorporation during cycling, is not resulting in the optimal composition with the highest lithium ion conductivity. The optimum lithium titanate

stoichiometry with the highest rate performance enhancement on CAMs has in fact been searched. E. g. Shim et $al.$ found a significantly improved rate performance for $Li_4Ti_5O_{12}$ compared to Li_2TiO_3 coated LCO.[18] Li_4TiO_4 and Li_2TiO_3 have been reported to have poor lithium ion conductivities.[34,35] The metastable phase $Li_2Ti_3O_7$ could also be an interesting candidate for coating of cathode materials. This ramsdellite-like phase exhibits a high lithium ion conductivity as polycrystalline material at room temperature,[36] but there is yet no report of its use as coating material. The strongly anisotropic lithium ion conductivity,[37] may be problematic for the coating properties, as the aggregates and the primary particles are typically randomly distributed. Consequently, the lithium ion conducting channels of $Li_2Ti_3O_7$ might probably not be oriented in the right direction. Our findings concerning the rate performance of the coated NMCs match well with the reported lithium ion conductivities for lithium aluminate, lithium zirconate and lithium titanate in literature. Lithium zirconate is ascribed a superior lithium ion conductivity than lithium titanate, which has a superior conductivity compared to lithium aluminate.[38,39]

In Figure S5, showing the discharge curves of the different applied discharge currents (C-rates) of all samples, it can be seen that the voltage plateau drops with increasing C-rates. This is caused by an increasing overpotential of the battery due to polarization effects in the electrodes, resulting into decreased discharge capacities.[40] In order to better understand this effect, the corresponding differential capacity (dQ/dV) plots are analyzed in detail (Figure 6). The peaks in the dQ/dV curves correspond to the plateaus in the charge/discharge profiles. All discharge curves shift towards lower potentials with increasing C-rates. In general, a change in polarization between the end of charge and the beginning of discharge (ECBD polarization) and a shift of the peak minimum is observed (marked in Figure 6). The polarization behavior between 0.1C and 4C is visualized in Figure 6h.

The observed trend of increasing polarization with increasing C-rate is uncoated NMC > TiO_2 > Al_2O_3 > $Li_4Zr_3O_8$ > $LiAlO_2$ > $Li_4Ti_5O_{12}$ > ZrO_2. For ZrO_2 coated NMC, the lowest ECBD polarization and peak minimum shift between 0.1C and 4C was observed, followed by $Li_4Ti_5O_{12}$ coated NMC, showing the second lowest polarization. $LiAlO_2$ coated NMC shows a slightly lower overall polarization compared to $Li_4Zr_3O_8$ coated NMC, which shows the lower peak polarization but an increased ECBD polarization. Al_2O_3 and TiO_2 coated NMC show almost identical ECBD polarization, but the peak minimum shift for the TiO_2 coated sample is significantly higher, even slightly higher than observed for uncoated NMC. The pristine NMC shows the highest ECBD polarization and overall polarization. Additionally, the peaks in discharge curves are becoming smaller and broader with increasing C-rate. The peak shrinking and broadening is less pronounced for those samples that showed lower shifts of the curves towards lower potentials. This indicates that also the shape of dQ/dV curves contains important information about the cycling behavior. The better the shape of the curve can be maintained at higher C-rates, the better the rate performance of the material.

The polarization is less pronounced for coated NMCs compared to uncoated NMC, revealing that the coatings help to maintain intercalation/deintercalation behavior with increasing discharge currents. The polarization and overpotential shifts of the individual coated NMCs match very well with the observed rate performances, indicating a very direct correlation between these parameters.

A long-term cycling test at a constant rate of 0.5C was performed after the rate test. Figure 5 shows the absolute capacity (Figure 5, top), as well as the normalized long-term cycling sequence for a better comparability (Figure 5, bottom: right). Galvanostatic charge and discharge profiles (rate of 0.5C) of the coated NMCs and uncoated NMC are demonstrated in Figure S6. It can be seen that the aluminum containing coating layers improve the stability and cycle life of NMC most effectively. Al_2O_3 and $LiAlO_2$ coated NMCs are performing very similar (capacity retention of 89% from cycle 25 to 100). In previous investigations, the strongest protecting effect, compared to ZrO_2 and TiO_2 coating layers, was also found for Al_2O_3 coatings due to favorable chemical properties, even when it did not show the highest coverage (physical parameter; the higher, the better the surface protection) of the reactive surface of the high-nickel NMC.[23] Here, the slightly higher surface coverage of Al_2O_3 and $LiAlO_2$ compared to the other coated NMCs (see Figure 3) is additionally contributing to the superior long-term cycling stability. Nevertheless, a superior absolute capacity is achieved for $LiAlO_2$ (147 mAh g^{-1} at cycle 100) compared to Al_2O_3 coated NMC (140 mAh g^{-1} at cycle 100). The second-best long-term stability, after the aluminum-containing samples, was obtained for $Li_4Ti_5O_{12}$ coated NMC (87% capacity retention from cycle 25 to 100, 145 mAh g^{-1} at cycle 100), closely followed by NMC with $Li_4Zr_3O_8$ coating (86% capacity retention from cycle 25 to 100, 134 mAh g^{-1} at cycle 100). $Li_4Zr_3O_8$ and $Li_4Ti_5O_{12}$ coated NMCs both show an improved long-term cycling stability compared to their lithium-free equivalents. A reason for this could be that the coating materials are predominantly accumulating on grain boundaries of the NMC surface (explained in more detail below). ZrO_2 coated NMC (capacity retention from cycle 25 to 100 = 82%, absolute capacity at cycle 100 = 131 mAh g^{-1}) is performing slightly better than TiO_2 coated NMC (capacity retention from cycle 25 to 100 = 80%; absolute capacity at cycle 100 = 121 mAh g^{-1}) in long-term cycling. In both cases, the coating agents are distributed more homogeneous over the whole surface of the CAM compared to their ternary analogues. Consequently, the more reactive grain boundaries are less covered. This could contribute to their inferior long-term cycling stability observed in the electrochemical evaluation part, and is further explained by a schematic model of CAM surface protection with fumed metal oxides in section 2.5. The uncoated NMC shows the lowest stability during long-term cycling, with only 74% capacity retention and an absolute capacity of 99 mAh g^{-1} at cycle 100.

In order to better understand the observed long-term cycling behavior and the voltage drop in the galvanostatic charge and discharge curves of the individual samples at prolonged cycling (Figure S6), the corresponding differential capacity plots of cycle 26 (beginning of long-term cycling sequence), cycle 50 and cycle 100 (end of test) are analyzed in detail in Figure 7. The peaks in the *dQ/dV* curves correspond to the plateaus in the galvanostatic charge/discharge profiles in Figure S6. The voltage region up to 3.8 V is almost similar for several NMC compositions, with anodic and cathodic peaks around 3.70-3.75 V, stemming from the hexagonal to monoclinic (H1 → M) phase transition of the NMC.[41]

During aging of a cell, characteristics in the corresponding differential capacity curves change in position, height and shape. These changes can be correlated to physical and chemical changes taking place inside the cell. As the electrochemical cycling proceeds, the curves change to a more polarized

state and shift further apart. There are three regions, where the polarization can be well observed: The charge peak shift (potential rise during cycling), the polarization between the end of charge and the beginning of discharge (ECBD polarization; increasing with prolonged cycling) and the discharge peak shift (potential drop during cycling).

The hysteresis between the charge and discharge curves is omnipresent in charge/discharge experiments of electrode materials and were explained by Goodenough *et al.*, who consider the potential of the charging step to be higher than that of the discharging step, caused by the polarization arising from the internal resistance of the electrode materials.[42] The discharge potential decreases due to this polarization below the open circuit voltage, and the charge potential increases to reverse the reaction on the electrode. During discharging, lithium ions intercalate into the interstitial space between the host lattices of the CAM and the transition metal d-orbitals function as electron acceptor, resulting in an decrease of energy and phase stabilization of the CAM.[40] To reverse the process, electrons and ions need to be promoted from these states of lower energy, which is consuming more energy.[40] Therefore, the energy of discharging a LIB is slightly lower than that during charging, leading to the potential gap between the charge and discharge curves.[40]
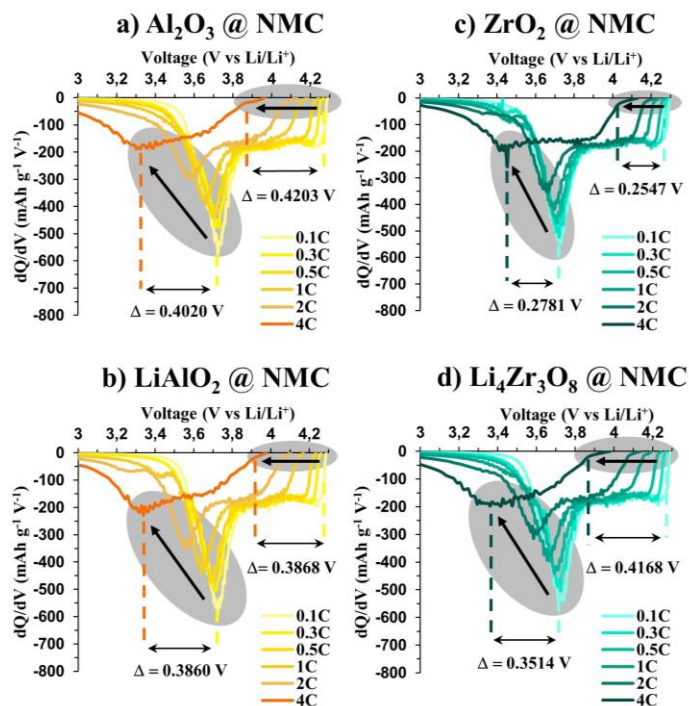
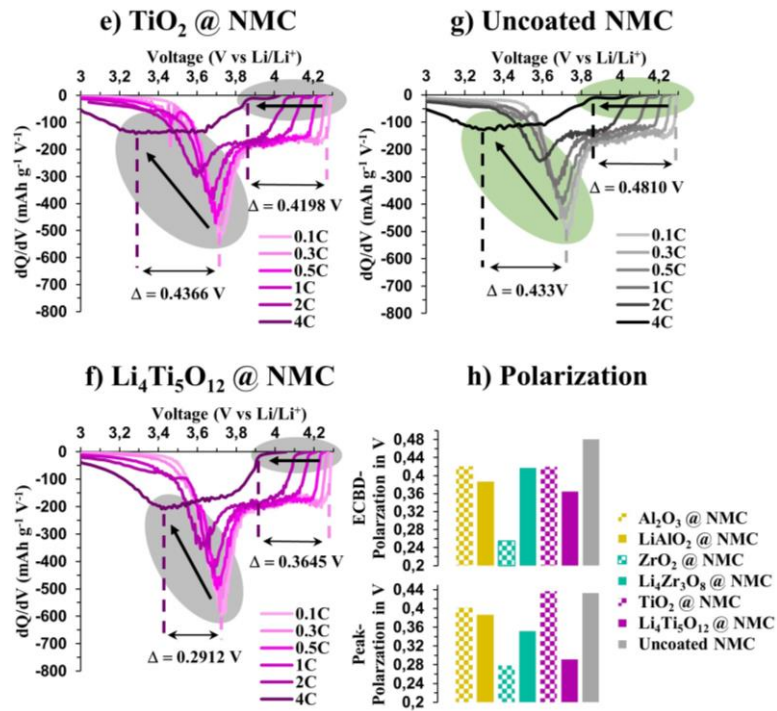*Figure 6.* a-g) *Differential capacity plots of the discharge curves for the individual discharge rates of the respective coated NMCs (a: Al₂O₃, b: LiAlO₂ c: ZrO₂ d: Li₄Zr₃O₈ e: TiO₂, f: Li₄Ti₅O₁₂) and uncoated NMC (g). h) Polarization evolution between 0.1C and 4C of the discharge peak and the polarization between the end of charge and the beginning of discharge (ECBD polarization).*
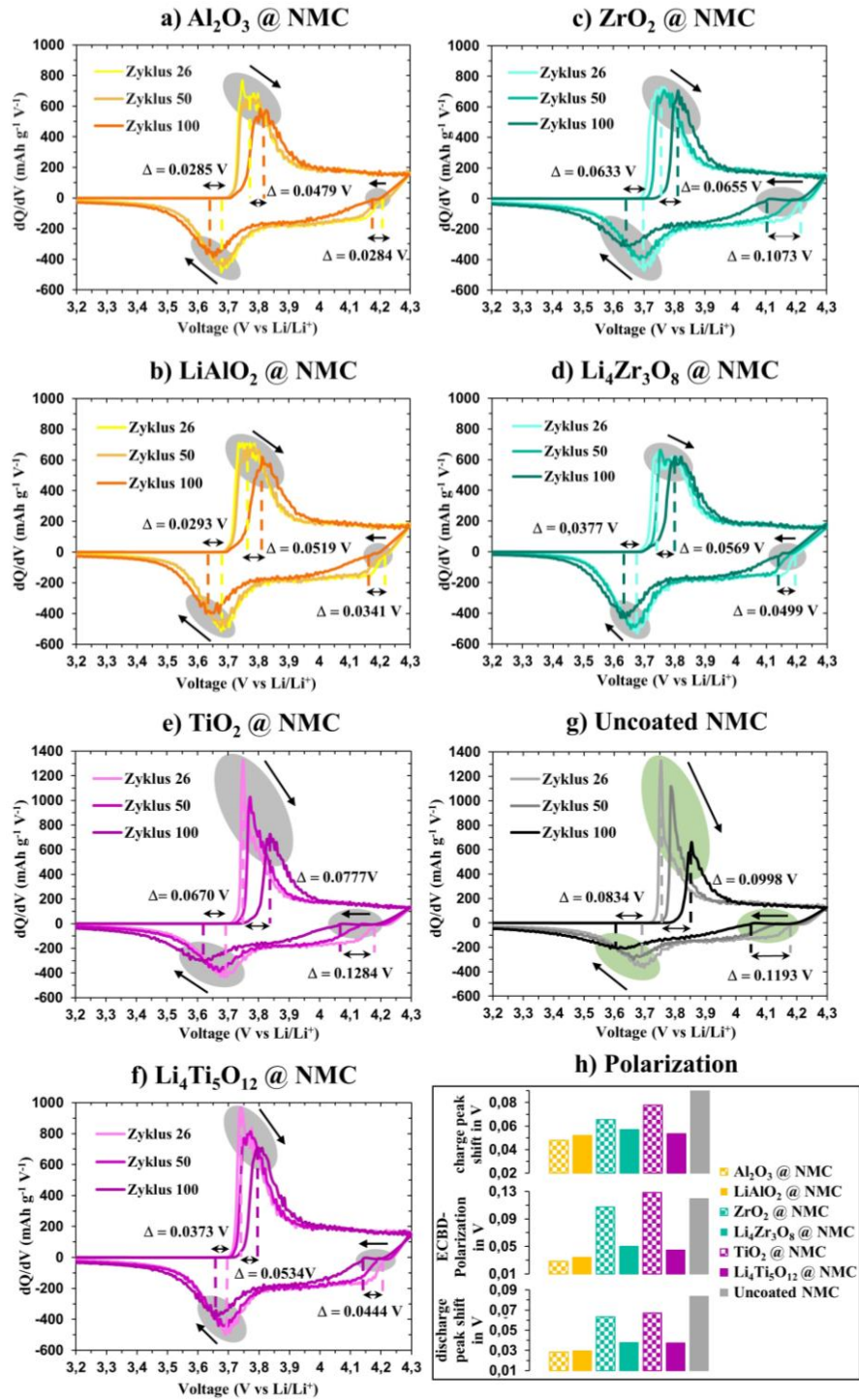
Figure 7. *a-g) Differential capacity plots of charge and discharge curves of the long-term cycling sequence of the respective coated NMCs (a: Al₂O₃, b: LiAlO₂ c: ZrO₂ d: Li₄Zr₃O₈ e: TiO₂, f: Li₄Ti₅O₁₂) and uncoated NMC (g). h) Polarization evolution between the first (cycle 26) and the last cycle (cycle 100) of the long term-cycling sequence for the individual samples, showing the charge peak shift, the polarization between the end of charge and the beginning of discharge (ECBD polarization) and the discharge peak shift.*

In general, the extent of polarization is closely linked to interfacial properties.[43] We understand that the shifts in peak position (potential) indicate an increase in internal resistance (IR) over the cell's life,[44] caused by interfacial side reactions (for detailed description see section 2.5). The polarization behaviors of the individual samples in the three mentioned areas of the *dQ/dV* curves

are demonstrated and compared in Figure 7h. Severe electrochemical polarization during prolonged cycling is obtained for uncoated NMC. In contrast, the electrochemical polarization evolution during cycling is reduced by all coatings, confirming that the fumed coating layers successfully prevent the contact between the reactive surface of the NMC and the electrolyte, since the polarization of the charge and discharge peaks and the increase in ECBD polarization can be attributed to parasitic side reactions of the cathode with the electrolyte.[45] The trend of polarization suppression and thus surface protection, for the coating materials is TiO_2 < ZrO_2 < $Li_4Zr_3O_8$ < $Li_4Ti_5O_{12}$ < $LiAlO_2$ ≈ Al_2O_3. This is accurately reflecting the observed trend for capacity retention during prolonged cycling. This again reveals that the polarization behavior correlates strongly with the capacities obtained in the cycling test.

The broadening and flattening of the peak shape indicate chemical changes of the battery materials. Apart from the shift, the redox peaks continuously broaden and flatten with cycling, this effect is mostly pronounced for uncoated NMC. This is attributed to the deterioration of the cathode/electrolyte interface, further explained in section 2.5.[45]

2.4 Characterization of cycled electrodes

SEM images of cross-sections of cycled electrodes are presented in Figure 8. The backscattered electrons (BSE) images nicely reveal the condition of the NMC particles after extensive cycling (250 cycles). The comparison of the BSE images with the corresponding EDX mappings of the respective coating metals allows conclusions to be drawn about how well the coating materials adhere to the surface of the NMC particles after cycling. In the images of the electrodes containing the fumed Al_2O_3 and $LiAlO_2$ coated NMC (Figure 8a+b), the NMC particles are still intact, almost no crack formation is observed after extensive cycling. The SEM-EDX mappings of Al disclose that the fumed Al_2O_3 and fumed $LiAlO_2$ are still around the surface of NMC particles and seem to adhere very well. In case of the ZrO_2, $Li_4Zr_3O_8$, TiO_2 and $Li_4Ti_5O_{12}$ coated NMCs (Figure 8c-f) a more pronounced crack formation can be observed. Hereby, the extent of crack formation is significantly stronger for the lithium-free coating agents. The EDX mappings of ZrO_2 and TiO_2 coated NMCs show that the coating material remained mostly on the NMC surface, but the presence of coating material in the space between the particles indicates that coating material is detached to a certain extent. We assume that, in the region where a crack forms and the particle breaks up, some small amount of coating material gets detached. $Li_4Zr_3O_8$ and $Li_4Ti_5O_{12}$ coated NMCs show moderate crack formation, while the coating materials remain at the NMC surface.
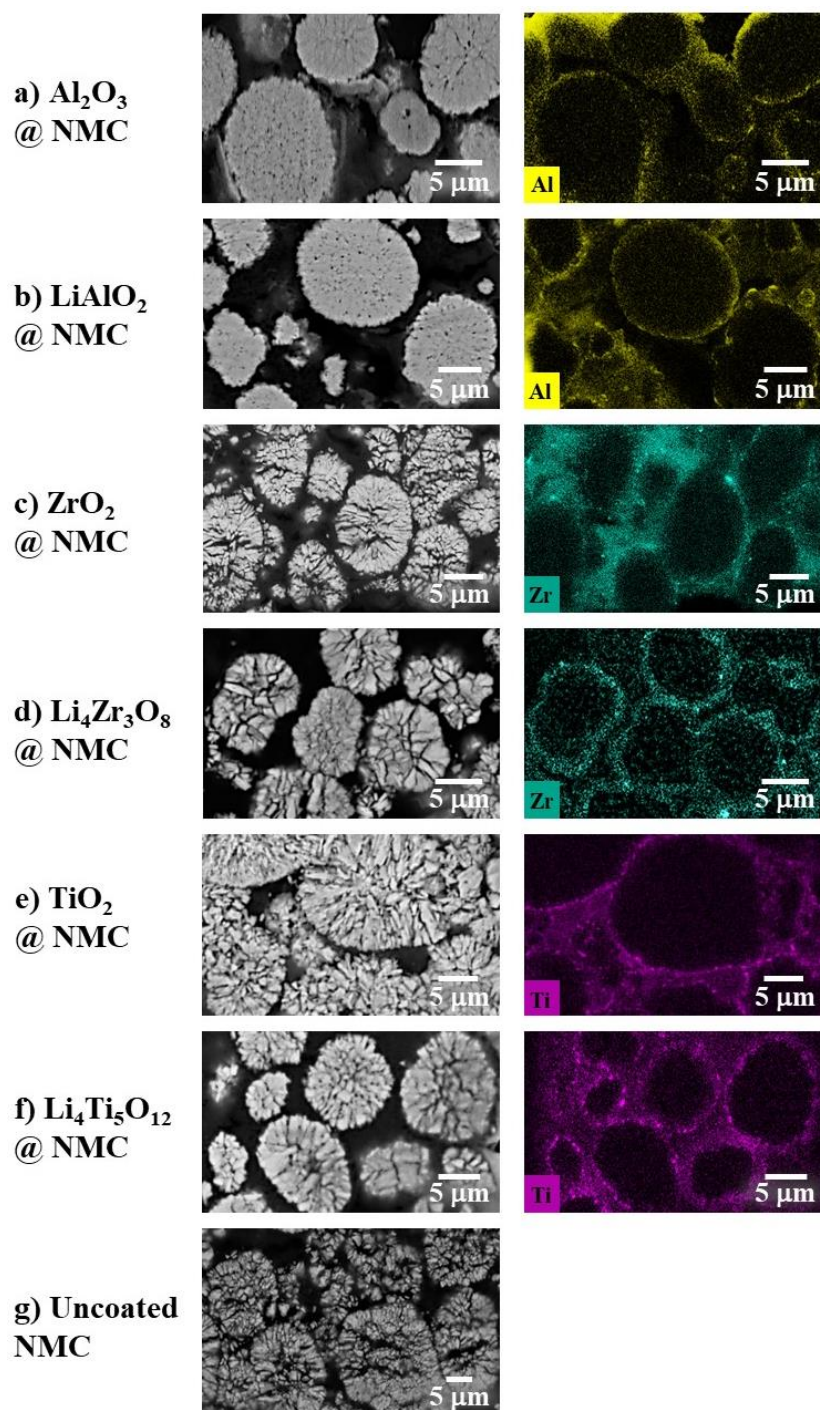
Figure 8. *SEM images of cross-sections of cycled NMC coated with the respective coating agent (a: Al_2O_3, b: $LiAlO_2$ c: ZrO_2 d: $Li_4Zr_3O_8$ e: TiO_2, f: $Li_4Ti_5O_{12}$) and uncoated NMC (g). The left side shows the respective BSE image and the right side presents the corresponding EDX mapping of the respective metal element of the coating material.*

For the uncoated reference sample, severe crack formation and particle degradation was detected after cycling (Figure 8g). The secondary particle structures fragmented almost completely into individual primary particles.

In summary, all dry coated fumed metal oxide layers remained almost intact, even after extensive battery cycling. For all coated NMCs, the crack formation and particle disintegration are

significantly less pronounced compared to the uncoated sample, demonstrating that these coating layers successfully protect high-nickel NMC from harmful side reactions. The coating materials prevent crack formation in the following order $LiAlO_2 \approx Al_2O_3 > Li_4Ti_5O_{12} > Li_4Zr_3O_8 > ZrO_2 > TiO_2$, which is consistent with the observed long-term cycling and polarization behavior improvement trend.

2.5 Schematic Model of Protection and Cycling Performance Improvement of CAMs by fumed metal oxides

To better understand how coating layers of fumed metal oxides protect high-nickel NMC from degradation and enhance its cycling performance, we sketched a schematic model (Figure 9). During cycling, high-nickel NMC materials suffer from several electrochemical degradation phenomena (Figure 9a-c). It is known that decomposition of electrolyte on the reactive NMC surface induces the persistent growth of a thick cathode electrolyte interface (CEI) layer with large resistance, resulting in an increased charge transfer resistance, consumption of the electrolyte and capacity degradation.[46,47] In addition, a thick CEI layer deteriorates the rate capability at high rates due to its low conductivity and lithium ion and electron blocking effect (Figure 9c).[48] The electron transport in the electrodes is, in addition to the lithium ion transport, an important factor influencing the rate performance.[33] Furthermore, the decomposition of commonly used $LiPF_6$ by the reaction with trace amounts of water reduces the conducting additive in the electrolyte and results in a release of corrosive HF, inactive LiF and species such as PO_xF_y.[49,50] The formed LiF layer on the electrode surface leads to a high resistance for lithium ion migration,[51] contributing to capacity and voltage fading. The highly acidic HF causes corrosion and dissolution of transition metals from the surface of the CAM and results in lattice damage (Figure 9b).[4,11,52] Surface layer transformations like the transition from layered to spinel and to a NiO-like rock-salt phase due to the reduction of Ni^{4+}, accompanied by oxygen loss and transition metal rearrangement destabilize the crystal structure, further increasing the resistance for lithium ions (Figure 9b).[7,8,49,53] Local chemical and physical inhomogeneities in cathodes lead to overcharge conditions caused by local inhomogeneities in current densities and SOC, resulting in highly delithiated regions.[54] Repulsive forces of adjacent transition metal oxide layers and the transformation to phases with enlarged lattice parameters cause anisotropic stress in highly delithiated areas.[55,56] Together with the usual volume change during (de)lithiation, this leads to discrete particle cracking, causing subsequent particle disintegration which is accompanied by capacity fading and increased polarization (Figure 7h) due to the loss of electronic contact (Figure 9c).[3,8,9,54,57] Due to a more pronounced impact of local inhomogeneities on local potentials and current densities, this degradation is significantly stronger with increasing C-rates .[54]
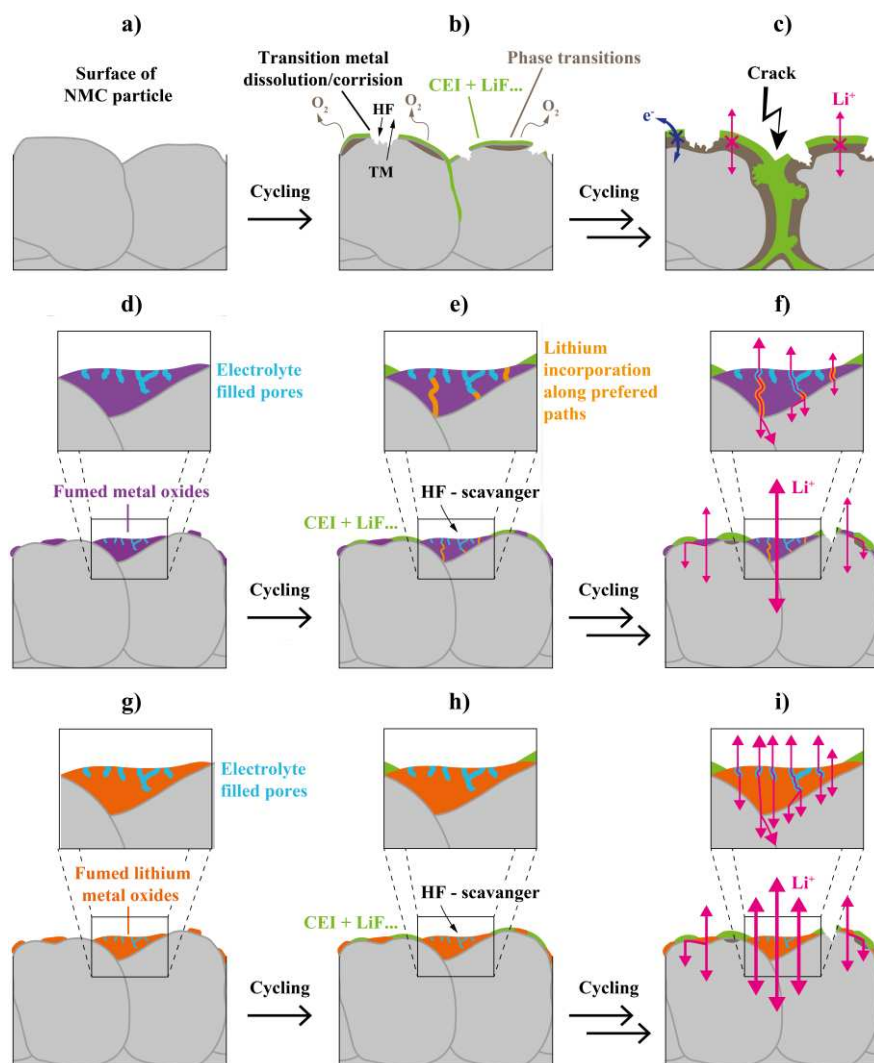
Figure 9. *Schematic model of how fumed metal oxide coatings protect high-nickel NMC from detrimental side reactions and enhance the cycling performance. Sections of uncoated NMC (a: before cycling, b: after moderate cycling, c: after extensive cycling), NMC coated with binary fumed metal oxides (d: before cycling, e: after moderate cycling, f: after extensive cycling) and NMC coated with ternary fumed lithium metal oxides (g: before cycling, h: after moderate cycling, i: after extensive cycling) show the proceeding phenomena and conditions of the respective material in different stages.*

Because of a low lithium ion diffusion energy barrier, lithium ions migrate preferably along grain boundaries in CAMs with secondary particle structure.[58,59] We therefore assume that also the reactivity with electrolyte species is there especially high. Furthermore, it is established that liquid electrolyte penetrates along the grain boundaries into the secondary particle structures.[60,61] The formation of a CEI layer along the grain boundaries of the cathode particles[62] and its thickening, as well as phase transformations with cation mixing is leading to increased mechanical stress in the secondary particles(Figure 9b,c).[60,63] During cycling, these heavily strained boundaries tend to cause intergranular cracking in the secondary particle structure (Figure 9c).[60,63] Prolonged cycling results in fracture along grain boundaries and subsequent collapse of the CAM secondary structures.[64] The resulting continuous increase in surface area, which is exposed to the electrolyte,

is creating more and more active sites for detrimental reactions, leading to self-amplification of the related side reactions.

The coating materials hinder the physical contact of the CAM surface and the electrolyte successfully and effectively suppress electrolyte decomposition, preventing the formation of a thick CEI (Figure 9d-i).[4,8,12] In only sparsely or uncovered areas on protruding particles (see Figure 3), it can be assumed that side reactions like the formation of a thin CEI and weak surface transformation at prolonged cycling cannot be completely prevented (Figure 9 e,f,h,i). Coated spots on the protruding particles surrounded by uncoated areas could act as a gateway for lithium ions due to the large resistance of the CEI formed on the uncoated areas. If the overall resistance is lower, the lithium ions migrate preferably via a coated area (gateway) and along the surface of the NMC instead of directly migrating through the CEI layer (Figure 9f,i). However, this should have rather minor effects on the cycling performance, as the lithium ions diffuse preferably along grain boundaries in the NMC secondary particle structure[58,59] and the entrances or exits of these vulnerable and important sites are well covered by the fumed coating agents (Figure 9d,g). This effect might be stronger for the materials that accumulate particularly pronounced in these reactive sites and form a denser coating in these areas (e.g. Al_2O_3, $LiAlO_2$, $Li_4Zr_3O_8$, $Li_4Ti_5O_{12}$). It can be estimated that coating material on top of grain boundaries hinders the penetration of liquid electrolyte to some extent. It is important to notice that, due to a certain densification and coalescence of the coating particles on the surface, the fumed metal oxide coating layers are not consistently porous (Figure 9d,g). Additionally, all of the here used coating materials can act as HF-scavenger[60,65,66] thus prevent the corrosion of the CAM and the dissolution of transition metals. Also, the diffusion of HF via the electrolyte inside the vulnerable grain boundaries is thus prevented (Figure 9e,h). The chemical ability of the coating material to protect the reactive NMC surfaces is thereby an important factor influencing the long-term cycling stability and cracking behavior. It was found that aluminum-containing coating materials have superior chemical properties to protect high-nickel NMC than zirconium- and titanium-containing species, which confirms previous investigations.[23] Furthermore, our coating layers seem to improve the conductivity of the cathode. This can be derived from the significant improvement in the rate capabilities of all coated samples, compared to the uncoated NMC. We attribute this effect to the suppression of the formation of lithium ion and electron blocking thick CEI layers. This should reduce local inhomogeneities in SOC and current densities in the electrode and may help to mitigate the correlated degradation.

The binary fumed metal oxides seem to incorporate lithium along preferred paths (Figure 9e).[23,24] These areas provide enhanced lithium ion diffusion and can act as channels for the passing lithium ions (Figure 9f). This is reducing the resistance of the normally insulating metal oxide layers, because the pure metal oxides possess a rather poor lithium ion conduction[18,21,67], and the lithium ions can migrate across the coating layer faster.[23,24] Penetration of liquid electrolyte in the partly porous coating layers (Figure 9d,g) contributes to an improved lithium ion diffusion to and from the NMC surface.[23,24] The lithium ion transport can then partly proceed through the filled pores by diffusion in liquid electrolyte (Figure 9f,i). This shortens the path the lithium ions have to diffuse through the coating material compared to a non-porous coating layer with the same thickness.

Therefore, the porosity of the coating layer reduces the effective coating layer thickness regarding the insulating effect of the coating materials. We suggest that the porosity of the coating layer has more significant influence on the lithium ion transport through the layer than the lithium ion diffusivities of the coating materials,[23] because the diffusion coefficients of the lithium metal oxides are orders of magnitude lower than that of liquid electrolyte.[38,39,68,69]

Using ternary lithium metal oxides as coating agents leads to a further improvement in rate capability. This is attributed to the improved lithium ion conductivity of the lithium containing materials, which were designed to the ideal stoichiometry for the highest lithium ion conduction. The lithium incorporation in the fumed binary metal oxides during cycling probably results not in the ideal composition. Furthermore, the ternary lithium metal oxides provide an enhanced lithium ion diffusion everywhere in the coating layer (Figure 9i), whereas in the binary fumed metal oxides the lithium conduction is only enhanced locally, where lithium was incorporated (Figure 9f).

In addition to these effects, the coating layers act as a kind of glue that holds the outer sphere of the secondary particle structure in place. This effect cannot be quantified, but should not be underestimated because the physical interactions are powerful enough to hold the dry-coated particles to the CAM surface, even under shear forces during the cathode fabrication process, including cathode slurry preparation and then calendering. Tsai *et al.*[70] showed that a thin binder layer on the surface is sufficient to prevent the decay that occurs in unconfined high-nickel CAM particles. Although radial cracks still occur, they are not opened to the particles surface and particle disintegration is not observable.

3. Conclusions

Nanostructured fumed Al_2O_3, ZrO_2, TiO_2, $LiAlO_2$, $Li_4Zr_3O_8$ and $Li_4Ti_5O_{12}$ were coated successfully on high-nickel NMC. Hereby, lithium-free binary and lithium-containing ternary coating agents can be processed equally in the dry powder high-energy mixing process. Fully and quite homogeneous coverage by the small aggregates around all CAM particles was achieved. The small nanostructured aggregate size is providing strong adhesion of the coating material on the CAM surface without a subsequent sintering step.

In previous investigations, it was found that lithium ions seem to incorporate in fumed Al_2O_3, ZrO_2 and TiO_2 during cycling, contributing to the improved lithium ion transport through the CAM surface layer of the normally insulating coating materials. Here, we showed that the use of ternary lithium metal oxide coating agents leads to further increased rate performance, long-term cycling stability and overall capacity, compared to their lithium-free binary coating equivalents, as long as the porosity of the coating layer is not reduced too much. It became apparent that the porosity of the coating layer is a physical parameter that significantly influences the rate capability, in addition to the lithium ion mobility in the coating material itself (chemical parameter). A high degree of coating layer porosity was found to be favorable for the rate capability and zirconium-containing coatings could be attributed the best chemical properties for high rate performances. Furthermore, a high coverage of the surface, especially in vulnerable grain boundaries, is enhancing the long-

term cycling stability and cracking behavior of NMC. Previous findings that the chemical nature of the coating material has significant impact on the cycling stability of NMC were confirmed. Aluminum-containing coatings could clearly be attributed to a superior chemical nature to protect high-nickel NMC.

All coatings effectively enhance the rate capability, capacity retention and polarization behavior during cycling. The observed trend for the increase in rate performance is: TiO_2 < Al_2O_3 < $Li_4Zr_3O_8$ < $LiAlO_2$ < $Li_4Ti_5O_{12}$ < ZrO_2 coated NMC. Please note that the rate capability of the $Li_4Zr_3O_8$ coated NMC is limited due to the reduced porosity of the coating, resulting from the lower BET-surface area of the coating material. We expect that the rate capability will be enhanced significantly when the BET value and thus the porosity of the coating can be increased. The trend in long-term cycling stability improvement is as follows: TiO_2 < ZrO_2 < $Li_4Zr_3O_8$ < $Li_4Ti_5O_{12}$ < $LiAlO_2$ ≈ Al_2O_3 coated NMC. Additionally, this trend was confirmed by SEM analyses of cross-sections of cycled electrodes, showing the same order in the propagation of crack formation. Finally, a schematic model was sketched, describing in detail how the fumed metal oxide coatings protect the surfaces of high-nickel NMC and enhance the cycling performance.

Summarizing, the highest rate capability was achieved by fumed ZrO_2-coating, while the best long-term cycling stability with the highest absolute capacity was obtained for NMC coated with fumed $LiAlO_2$. Fumed $Li_4Ti_5O_{12}$ would be the optimal coating agent for NMC to achieve a balanced system, providing a good compromise between both, a high rate capability and a good capacity retention.

We like to add that the dry coating approach of cathode active materials in a high-energy mixer is easily up-scalable and therefore well suitable for industrial use. The use of lithium ion conductive coating agents is not only very promising for enhancing the cycling performance in liquid cells, but also opens a new strategy for coating of cathode materials applied in solid-state batteries.

4. Experimental

For this study, commercial NMC701515 powder (from Linyi Gelon LIB Co.) and fumed Al_2O_3, ZrO_2, TiO_2, $LiAlO_2$, $Li_4Zr_3O_8$ and $Li_4Ti_5O_{12}$ ("AEROXIDE® Alu 65", "VP ZrO_2", "AEROXIDE® TiO_2 P25", "VP LAO", "VP LZO", "VP LTO" from EVONIK OPERATIONS GmbH) were used. To conduct the dry powder coating process, a lab scale high-intensity mixer from SOMAKON VERFAHRENSTECHNIK UG (SOMAKON mixer MP-GL) was used with a mixing unit consisting of two high-speed rotating rotors with 4 blades each and a volume of 0.5 L. The coating approach can also be transferred to large-scale mixers for industrial use (e.g. from EIRICH GmbH up to a mixer size of 3000 L). The NMC powder was mixed with 1.0 wt-% of the respective fumed metal oxide in the high-intensity mixer for 1 min at 500 rpm. Afterwards the mixing speed was raised to 2000 rpm for 6 min for the de-agglomeration of the fumed metal oxide agglomerates into smaller aggregates that interact with the NMC surface. No additional sinter step was proceeded, the coated cathode material was used as obtained after dry mixing.

Characterization

Scanning electron microscopy (SEM). For SEM investigations, the "JSM-7600F" microscope from JEOL was used. The accelerating voltage was set to 1 kV, and the beam current to 30 pA. To fix the samples on the sample holders, a graphite tape was used. Electron-dispersive X-ray spectroscopy (EDX) analysis was operated with a X-MAX 150 mm^2 detector (from OXFORD INSTRUMENTS) and processed with AZTEC-software. The accelerating voltage and beam current were increased for these measurements to 20 kV and 500 pA, respectively. Cross-sections of cycled electrodes were prepared by using a cross-section polisher from JEOL (Cryo-Cross-Section-Polisher CCSP, Modell IB 19520 CCP). The samples were stacked in between two silicon wafers and subsequently cut with an argon ion beam (-80 °C, 5 kV, 8h).

X-ray powder diffraction (XRD). XRD measurements were performed with a CUBIX3 PHARMA diffractometer and a X'CELERATOR detector. To investigate the crystal structure of the powders, Cu-K$_\alpha$ radiation was employed. A 2θ range from 5° to 100° with a step size of 0.02° and a count time of 40 s was applied.

BET surface area. Single point BET surface area measurements were performed with a MICROMERITICS TRISTAR 3000 with a nitrogen/helium flow (28.6% N$_2$). Before the measurement, the samples were heated to 150 °C for 20 min for degassing.

Transmission Electron Microscopy (TEM): For cutting the cross-sectional TEM lamellae out of the respective coated spherical NMC samples, a FEI HELIOS 650 dual-beam Focused Ion Beam device was used. Carbon and platinum protective layers were deposited on top of the film to protect the samples during the cutting process. Probe aberration corrected high angular annual dark field scanning transmission electron microscopy (HAADF-STEM) and energy dispersive X-ray spectroscopy (EDX) were conducted on a probe aberration-corrected FEI TITAN^3 80-300 electron microscope equipped with SUPER-X EDX detector system operated at 300 kV. For high resolution (HR) TEM images and electron energy loss spectroscopy (EELS) analysis, a double aberration-corrected FEI TITAN^3 80-300 electron microscope was used. For this measurements, the device was operated at 300 kV in monochromated mode providing an energy resolution of 150 meV. Each specimen was cleaned through beam shower using a large parallel beam with a beam current of 14 nA before the TEM experiments.

Electrode and Cell Preparation. For electrochemical measurements, electrodes were prepared by blending 90 wt-% NMC with 5 wt-% PVDF (SOLEF PVDF 5130) and 5 wt-% SUPER PLi (TIMCAL) in N-Methyl-2-Pyrrolidone (NMP) under argon atmosphere. The slurry was casted on aluminum foil and dried in air for 20 min on a 120 °C heating plate. Afterwards, the electrode sheet was further dried in vacuum for 2 h at 120 °C. Circular electrodes with a diameter of 12 mm were punched out and calendered with a pressure of 620 kPa. The electrodes are dried again in vacuum for 12 h at 120 °C to remove any residual NMP and moisture. The cathode loading was set to 1.3-1.4 mAh cm^{-2} (assuming a specific capacity of 180 mAh g^{-1} at a rate of 1C) or 7.0 - 8.0 mg$_{NMC}$ cm^{-2}.

CR2032-type coin cells (MTI Corporation) were assembled under argon atmosphere. As anode material, lithium metal (Rockwood Lithium GmbH) was used and Celgard 2500 was used as separator. As electrolyte, 25 μL of a 1 molar solution of $LiPF_6$ in ethylene carbonate and ethyl methyl carbonate (50:50 wt/wt; Sigma-Aldrich) was used. The coin cells were locked with a crimper (MTI).

Cell cycling. Galvanostatic cell cycling was conducted between 3.0 and 4.3 V vs. Li^+/Li at room temperature with a MACCOR battery cycler. Only the active material mass was considered for the calculation of the capacities and the specific currents. The C-rate was raised every four cycles during cycling, starting from 0.1/0.1C (Charge/Discharge) to 0.3/0.3C, 0.5/0.5C, 1.0/1.0C, 1.0/2.0C and 1.0/4.0C. Afterwards, for the long-term stability investigations, the cells were cycled at 0.5/0.5C.

Supporting Information

XRD patterns of coating materials unknown to literature and uncoated as well as coated NMCs; HAADF-STEM Z-contrast images and STEM-EDX analysis of cross-sections of coated NMCs; ELNES-spectra/fine structures of coating materials before coating and after coating; Galvanostatic discharge profiles of uncoated and coated samples.

Acknowledgments

References

[1]   Yabuuchi, N.; Ohzuku, T. Novel lithium insertion material of $LiCo_{1/3}Ni_{1/3}Mn_{1/3}O_2$ for advanced lithium-ion batteries. *J. Power Sources* **2003**, *119-121*, 171–174.

[2]   De Biasi, L.; Kondrakov, A. O.; Geßwein, H.; Brezesinski, T.; Hartmann, P.; Janek, J. Between Scylla and Charybdis: Balancing Among Structural Stability and Energy Density of Layered NCM Cathode Materials for Advanced Lithium-Ion Batteries. *J. Phys. Chem. C* **2017**, *121*, 26163–26171.

[3]   Liu, W.; Oh, P.; Liu, X.; Lee, M.-J.; Cho, W.; Chae, S.; Kim, Y.; Cho, J. Nickel-Rich Layered Lithium Transition-Metal Oxide for High-Energy Lithium-Ion Batteries. *Angew. Chem. Int. Ed.* **2015**, *54*, 4440–4457.

[4]   Mauger, A.; Julien, C. Surface modifications of electrode materials for lithium-ion batteries: status and trends. *Ionics* **2014**, *20*, 751–787.

[5]   Jung, S.-K.; Gwon, H.; Hong, J.; Park, K.-Y.; Seo, D.-H.; Kim, H.; Hyun, J.; Yang, W.; Kang, K. Understanding the Degradation Mechanisms of $LiNi_{0.5}Co_{0.2}Mn_{0.3}O_2$ Cathode Material in Lithium Ion Batteries. *Adv. Energy Mater.* **2014**, *4*, 1300787.

[6]   Wu, B.; Bi, J.; Liu, Q.; Mu, D.; Wang, L.; Fu, J.; Wu, F. Role of current density in the degradation of $LiNi_{0.6}Co_{0.2}Mn_{0.2}O_2$ cathode material. *Electrochimica Acta* **2019**, *298*, 609–615.

[7]   Lee, K.-S.; Myung, S.-T.; Amine, K.; Yashiro, H.; Sun, Y.-K. Structural and Electrochemical Properties of Layered $Li[Ni_{1–2x}Co_xMn_x]O_2$ (x = 0.1–0.3) Positive Electrode Materials for Li-Ion Batteries. *J. Electrochem. Soc.* **2007**, *154*, A971.

[8]   De Biasi, L.; Schwarz, B.; Brezesinski, T.; Hartmann, P.; Janek, J.; Ehrenberg, H. Chemical, Structural, and Electronic Aspects of Formation and Degradation Behavior on Different Length Scales of Ni-Rich NCM and Li-Rich HE-NCM Cathode Materials in Li-Ion Batteries. *Adv. Mater.* **2019**, *31*, 1900985.

[9]   Mohanty, D.; Dahlberg, K.; King, D. M.; David, L. A.; Sefat, A. S.; Wood, D. L.; Daniel, C.; Dhar, S.; Mahajan, V.; Lee, M.; Albano, F. Modification of Ni-Rich FCG NMC and NCA Cathodes by Atomic Layer Deposition: Preventing Surface Phase Transitions for High-Voltage Lithium-Ion Batteries. *Sci Rep* **2016**, *6*, 26532.

[10] Cabana, J.; Kwon, B. J.; Hu, L. Mechanisms of Degradation and Strategies for the Stabilization of Cathode–Electrolyte Interfaces in Li-Ion Batteries. *Acc. Chem. Res.* **2018**, *1*, 299–308.

[11] Oh, Y.; Nam, S.; Wi, S.; Hong, S.; Park, B. Nanoscale interface control for high-performance Li-ion batteries. *Electron. Mater. Lett.* **2012**, *8*, 91–105.

[12] Zuo, D.; Tian, G.; Li, X.; Chen, D.; Shu, K. Recent progress in surface coating of cathode materials for lithium ion secondary batteries. *J. Alloys Compd.* **2017**, *706*, 24–40.

[13] Chen, C.; Tao, T.; Qi, W.; Zeng, H.; Wu, Y.; Liang, B.; Yao, Y.; Lu, S.; Chen, Y. High-performance lithium ion batteries using SiO_2-coated $LiNi_{0.5}Co_{0.2}Mn_{0.3}O_2$ microspheres as cathodes. *J. Alloys Compd.* **2017**, *709*, 708–716.

[14] Dong, S.; Zhou, Y.; Hai, C.; Zeng, J.; Sun, Y.; Shen, Y.; Li, X., Ren, X.; Qi, G.; Zang, X.; Ma, L. Ultrathin CeO_2 coating for improved cycling and rate performance of Ni-rich layered $LiNi_{0.7}Co_{0.2}Mn_{0.1}O_2$ cathode materials. *Ceram. Int.* **2019**, *45*, 144–152.

[15] Yoo, K. S.; Kang, Y. H.; Im, K. R.; Kim, C.-S. Surface modification of NMC 622 Cathode materials by nano-Al_2O_3 to improve electrochemical performance in lithium ion batteries. *Materials* **2017**, *10*, 1273.

[16] Chen, Y.; Zhang, Y.; Chen, B.; Wang, Z.; Lu, C. An approach to application for $LiNi_{0.6}Co_{0.2}Mn_{0.2}O_2$ cathode material at high cutoff voltage by TiO_2 coating. *J. Power Sources* **2014**, *256*, 20–27.

[17] Yano, A.; Ueda, A.; Shikano, M.; Sakaebe, H.; Ogumi, Z. Surface Structure and High-Voltage Charging/Discharging Performance of Low-Content Zr-Oxide-Coated $LiNi_{1/3}Co_{1/3}Mn_{1/3}O_2$. *J. Electrochem. Soc.* **2016**, *163*, A75–A82.

[18] Shim, J.-H.; Lee, J.; Han, S. Y.; Lee, S. Synergistic effects of coating and doping for lithium ion battery cathode materials: synthesis and characterization of lithium titanate-coated $LiCoO_2$ with Mg doping. *Electrochimica Acta* **2015**, *186*, 201–208.

[19] Sun, S.; Du, C.; Qu, D.; Zhang, X.; Tang, Z. Li_2ZrO_3-coated $LiNi_{0.6}Co_{0.2}Mn_{0.2}O_2$ for high-performance cathode material in lithium-ion battery. *Ionics* **2015**, *21*, 2091–2100.

[20] Heo, K.; Lee, J.-S.; Kim, H.-S.; Kim, J.; Lim, J. Enhanced Electrochemical Performance of Ionic-Conductor Coated $Li[Ni_{0.7}Co_{0.15}Mn_{0.15}]O_2$. *J. Electrochem. Soc.* **2017**, *164*, A2398–A2402.

[21] Liu, W.; Li, X.; Xiong, D.; Hao, Y.; Li, J.; Kou, H.; Yan, B.; Li, D.; Lu, S.; Koo, A.; Adair, K.; Sun, X. Significantly improving cycling performance of cathodes in lithium ion batteries: The effect of Al_2O_3 and $LiAlO_2$ coatings on $LiNi_{0.6}Co_{0.2}Mn_{0.2}O_2$. *Nano Energy* **2018**, *44*, 111–120.

[22] Laskar, M. R.; Jackson, D. H. K.; Xu, S.; Hamers, R. J.; Morgan, D.; Kuech, T. F. Atomic Layer Deposited MgO: A Lower Overpotential Coating for $Li[Ni_{0.5}Mn_{0.3}Co_{0.2}]O_2$ Cathode. *ACS Appl. Mater. Interfaces* **2017**, *9*, 11231–11239.

[23] Herzog, M. J.; Esken, D.; Janek, J. Improved Cycling Performance of High-Nickel NMC by Dry Powder Coating with Nanostructured Fumed Al_2O_3, TiO_2, and ZrO_2: A Comparison. *Batter. Supercaps* **2021**, doi:10.1002/batt.202100016.

[24] Herzog, M. J.; Gauquelin, N.; Esken, D.; Verbeeck, J.; Janek, J. Facile dry coating method of high-nickel cathode material by nanostructured fumed alumina (Al_2O_3) improving the performance of lithium-ion batteries. *Energy Technol.* **2021**, DOI 10.1002/ente.202100028.

[25] Albers, P.; Maier, M.; Reisinger, M.; Hannebauer, B.; Weinand, R. Physical boundaries within aggregates - differences between amorphous, para-crystalline, and crystalline Structures. *Cryst. Res. Technol.* **2015**, *50*, 846–865.

[26] Wang, D.; Liu, L.; Sun, X.; Sham, T.-K. Observation of lithiation-induced structural variations in TiO_2 nanotube arrays by X-ray absorption fine structure. *J. Mater. Chem. A* **2015**, *3*, 412–419.

[27] Bouchet, D.; Colliex, C. Experimental study of ELNES at grain boundaries in alumina: intergranular radiation damage effects on $Al-L_{23}$ and O-K edges. *Ultramicroscopy* **2003**, *96*, 139–152.

[28] Jia, Y.; He, G.; Hu, W.; Yang, H.; Yang, Z.; Yu, H.; Zhang, Q.; Shi, J.; Lin, Z.; Yuan, J.; Zhu, B.; Gu, L.; Li, H.; Jin, K. The effects of oxygen in spinel oxide $Li_{1+x}Ti_{2-x}O_{4-\delta}$ thin films. *Sci. Rep.* **2018**, *8*, 3995.

[29] Kitta, M.; Akita, T.; Tanaka, S.; Kohyama, M. Characterization of two phase distribution in electrochemically-lithiated spinel $Li_4Ti_5O_{12}$ secondary particles by electron energy-loss spectroscopy. *J. Power Sources* **2013**, *237*, 26–32.

[30] Singh, B.; Gupta, M. K.; Mittal, R.; Chaplot, S. L. Phonons, phase transitions and thermal expansion in $LiAlO_2$: an *ab initio* density functional study. *Phys. Chem. Chem. Phys.* **2018**, *20*, 12248–12259.

[31] Jung, R.; Morasch, R.; Karayaylali, P.; Phillips, K.; Maglia, F.; Stinner, C.; Shao-Horn, Y.; Gasteiger, H. A. Effect of Ambient Storage on the Degradation of Ni-Rich Positive Electrode Materials (NMC811) for Li-Ion Batteries. *J. Electrochem. Soc.* **2018**, *165*, A132–A141.

[32] Sicklinger, J.; Metzger, M.; Beyer, H.; Pritzl, D.; Gasteiger, H. A. Ambient Storage Derived Surface Contamination of NCM811 and NCM111: Performance Implications and Mitigation Strategies. *J. Electrochem. Soc.* **2019**, *166*, A2322–2335.

[33] Tian, R.; Park, S.-H.; King, P. J.; Cunningham, G.; Coelho, J.; Nicolosi, V.; Coleman, J. N. Quantifying the factors limiting rate performance in battery electrodes. *Nat. Commun.* **2019**, *10*, 1933.

[34] Vijayakumar, M.; Kerisit, S.; Yang, Z.; Graff, G. L.; Liu, J.; Sears, J. A.; Burton, S. D.; Rosso, K. M.; Hu, J. Combined ^{6,7}Li NMR and Molecular Dynamics Study of Li Diffusion in Li_2TiO_3. *J. Phys. Chem. C* **2009**, *113*, 20108–20116

[35] Dissanayake, M. A. K. L.; Gunawardane, R. P.; Sumathipala, H. H.; West, A. R. New solid electrolytes and mixed conductors: $Li_{3+x}Cr_{1-x}M_xO_4$: M=Ge, Ti. *Solid State Ionics* **1995**, *76*, 215–220.

[36] Boyce, J. B.; Mikkelsen, J. C. ANISOTROPIC CONDUCTIVITY IN A CHANNEL-STRUCTURED SUPERIONIC CONDUCTOR: $Li_2Ti_3O_7$. *Solid State Communications* **1979**, *31*, 741–745.

[37] Wiedemann, D.; Nakhal, S.; Franz, A.; Lerch, M. Lithium diffusion pathways in metastable ramsdellite-like $Li_2Ti_3O_7$ from high-temperature neutron diffraction. *Solid State Ion.* **2016**, *293*, 37–43.

[38] Uhlendorf, J.; Ruprecht B.; Witt, E.; Chandran, C. V.; Dörrer, L.; Hüger, E.; Strauß, F.; Heitjans, P.; Schmidt, H. Slow Lithium Transport in Metal Oxides on the Nanoscale. *Z. Für Phys. Chem.* **2017**, *231*, 1423–1442.

[39] Dong, Y.; Zhao, Y.; Duan, H.; Huang, J. Electrochemical performance and lithium-ion insertion/extraction mechanism studies of the novel Li_2ZrO_3 anode materials. *Electrochimica Acta* **2015**, *161*, 219–225.

[40] Liu, C.; Neale, Z. G.; Cao, G. Understanding electrochemical potentials of cathode materials in rechargeable batteries. *Materials Today* **2016**, *19*, 109–123.

[41] Jung, R.; Metzger, M.; Maglia, F.; Stinner, C.; Gasteiger, H. A. Oxygen Release and Its Effect on the Cycling Stability of $LiNi_xMn_yCo_zO_2$ (NMC) Cathode Materials for Li-Ion Batteries. *J. Electrochem. Soc.* **2017**, *164*, A1361.

[42] Goodenough, J. B.; Park, K.-S. The Li-Ion Rechargeable Battery: A Perspective. *J. Am. Chem. Soc.* **2013**, *135*, 1167–1176.

[43] Lei, B.; Yang, J.; Xu, Z.; Su, S.; Wang, D.; Fumed alumina induced gel-like electrolyte for great performance improvement of lithium-sulfur batteries. *Chem. Commun.* **2018**, *54*, 13567–13570.

[44] Noh, H.-J.; Youn, S.; Yoon, C. S.; Sun, Y.-K. Comparison of the structural and electrochemical properties of layered $Li[Ni_xCo_yMn_z]O_2$ (*x* = 1/3, 0.5, 0.6, 0.7, 0.8 and 0.85) cathode material for lithium-ion batteries. *J. Power Sources* **2013**, *233*, 121–130.

[45] Negi, R. S.; Culver, S. P.; Mazilkin, A.; Brezesinski, T.; Elm, M. T. Enhancing the Electrochemical Performance of $LiNi_{0.70}Co_{0.15}Mn_{0.15}O_2$ Cathodes Using a Practical Solution-Based Al_2O_3 Coating. *ACS Appl. Mater. Interfaces* **2020**, *12*, 31392–31400.

[46] Liu, X.-H.; Kou, L.-Q.; Shi, T.; Liu, K.; Chen L. Excellent high rate capability and high voltage cycling stability of Y_2O_3-coated $LiNi_{0.5}Co_{0.2}Mn_{0.3}O_2$. *J. Power Sources* **2014**, *267*, 874–880.

[47] Shim, J.; Kostecki, R.; Richardson, T.; Song, X.; Striebel, K. A. Electrochemical analysis for cycle performance and capacity fading of a lithium-ion battery cycled at elevated temperature. *J. Power Sources* **2002**, *112*, 222–230.

[48] Jo, M.; Hong, Y.-S.; Choo, J.; Cho, J. Effect of $LiCoO_2$ Cathode Nanoparticle Size on High Rate Performance for Li-Ion Batteries. *J. Electrochem. Soc.* **2009**, *156*, A430.

[49] Duan, J.; Tang, X.; Dai, H.; Yang, Y.; Wu, W.; Wei, X.; Huang, Y. Building Safe Lithium-Ion Batteries for Electric Vehicles: A Review. *Electrochem. Energ. Rev.* **2020**, *3*, 1–42.

[50] Xu, K. Electrolytes and Interphases in Li-Ion Batteries and Beyond. *Chem. Rev.* **2014**, *114*, 11503–11618.

[51] Gnanaraj, J. S.; Zinigrad, E.; Levi, M. D.; Aurbach, D.; Schmidt, M. A comparison among $LiPF_6$, $LiPF_3(CF_2CF_3)_3$ (LiFAP), and $LiN(SO_2CF_2CF_3)_2$ (LiBETI) solutions: electrochemical and thermal studies. *J. Power Sources* **2003**, *119-121*, 799–804.

[52] Tebbe, J. L.; Holder, A. M.; Musgrave, C. B. Mechanisms of $LiCoO_2$ Cathode Degradation by Reaction with HF and Protection by Thin Oxide Coatings. *ACS Appl. Mater. Interfaces* **2015**, *7*, 24265–24278.

[53] Bak, S.-M.; Hu, E.; Zhou, Y.; Yu, X.; Senanayake, S. D.; Cho, S.-J.; Kim, K.-B.; Chung, K. Y.; Yang, X.-Q.; Nam, K.-W. Structural Changes and Thermal Stability of Charged $LiNi_xMn_yCo_zO_2$ Cathode Materials Studied by Combined *In Situ* Time-Resolved XRD and Mass Spectroscopy. *ACS Appl. Mater. Interfaces* **2014**, *6*, 22594–22601.

[54] Börner, M.; Horsthemke, F.; Kollmer, F.; Haseloff, S.; Friesen, A.; Niehoff, P.; Nowak, S.; Winter, M.; Schappacher, F. M. Degradation effects on the surface of commercial $LiNi_{0.5}Co_{0.2}Mn_{0.3}O_2$ electrodes. *J. Power Sources* **2016**, *335*, 45–55.

[55] Hwang, S.; Chang, W.; Kim, S. M.; Su, D.; Kim, D. H.; Lee, J. Y.; Chung, K. Y.; Stach, E. A. Investigation of Changes in the Surface Structure of $Li_xNi_{0.8}Co_{0.15}Al_{0.05}O_2$ Cathode Materials Induced by the Initial Charge. *Chem. Mater.* **2014**, *26*, 1084–1092.

[56] Julien, C. Local cationic environment in lithium nickel–cobalt oxides used as cathode materials for lithium batteries. *Solid State Ionics* **2000**, *136–137*, 887–896.

[57] Schweidler, S.; de Biasi, L.; Garcia, G.; Mazilkin, A.; Hartmann, P.; Brezesinski, T.; Janek, J. Investigation into Mechanical Degradation and Fatigue of High-Ni NCM Cathode Material: A Long-Term Cycling Study of Full Cells. *ACS Appl. Energy Mater.* **2019**, *2*, 7375–7384.

[58] Moriwake, H.; Kuwabara, A.; Fisher, C. A. J.; Huang, R.; Hitosugi, T.; Ikuhara Y. H.; Oki, H.; Ikuhara, Y. First-Principles Calculations of Lithium-Ion Migration at a Coherent Grain Boundary in a Cathode Material, $LiCoO_2$. *Adv. Mater.* **2013**, *25*, 618–622.

[59] Han, S.; Park, J.; Lu, W.; Sastry, A. M. Numerical study of grain boundary effect on Li^+ effective diffusivity and intercalation-induced stresses in Li-ion battery active materials. *J. Power Sources* **2013**, *240*, 155–167.

[60] Xiao, B.; Sun, X. Surface and Subsurface Reactions of Lithium Transition Metal Oxide Cathode Materials: An Overview of the Fundamental Origins and Remedying Approaches. *Adv. Energy Mater.* **2018**, *8*, 1802057.

[61] Yang, P.; Zheng, J.; Kuppan, S.; Li, Q.; Xiao, J.; Chen, G.; Zhang, J.-G.; Wang, C.-M. Phosphorus Enrichment as a New Composition in the Solid Electrolyte Interphase of High-Voltage Cathodes and Its Effects on Battery Cycling. *Chem. Mater.* **2015**, *27*, 7447–7451.

[62] Yan, P.; Zheng, J.; Liu, J.; Wang, B.; Sun, X.; Wang, C.; Zhang, J.-G. Tailoring grain boundary structures and chemistry of Ni-rich layered cathodes for enhanced cycle stability of lithium-ion batteries. *Nature Energy* **2018**, *3*, 600–605.

[63] Sharifi-Asl, S.; Yurkiv, V.; Gutierrez, A.; Cheng, M.; Balasubramanian, M.; Mashayek, F.; Croy, J.; Shahbazian-Yassar, R. Revealing Grain-Boundary-Induced Degradation Mechanisms in Li-Rich Cathode Materials. *Nano Lett.* **2020**, *20*, 1208–1217.

[64] Schipper, F.; Erickson, E. M.; Erk, C.; Shin, J.-Y.; Chesneau, F. F.; Aurbach, D. Review—Recent Advances and Remaining Challenges for Lithium Ion Battery Cathodes. *J. Electrochem. Soc.* **2017**, *164*, A6220–A6221.

[65] Aykol, M.; Kirklin, S.; Wolverton, C. Thermodynamic Aspects of Cathode Coatings for Lithium-Ion Batteries. *Adv. Energy Mater.* **2014**, *4*, 1400690.

[66] Haridas, A. K.; Nguyen, Q. A.; Song, B. F.; Blaser, R.; Biswal, S. L. ALD-Modified $LiNi_{0.33}Mn_{0.33}Co_{0.33}O_2$ Paired with Macroporous Silicon for Lithium-Ion Batteries: An Investigation on Lithium Trapping, Resistance Rise, and Cycle-Life Performance. *ACS Appl. Energy Mater.* **2020**, *3*, 456–468.

[67] Zhang, J.; Li, Z.; Gao, R.; Hu, Z.; Liu, X. High Rate Capability and Excellent Thermal Stability of Li^+-Conductive Li_2ZrO_3-Coated $LiNi_{1/3}Co_{1/3}Mn_{1/3}O_2$ via a Synchronous Lithiation Strategy. *J. Phys. Chem. C* **2015**, *119*, 20350–20356.

[68] Lee, S.-I.; Jung, U.-H.; Kim, Y.-S.; Kim, M.-H.; Ahn, D.-J.; Chun, H.-S. A Study of Electrochemical Kinetics of Lithium Ion in Organic Electrolytes. *Korean J. Chem. Eng.* **2002**, *19*, 638–644.

[69] Stewart, S. G.; Newman, J. The Use of UV/vis Absorption to Measure Diffusion Coefficients in $LiPF_6$ Electrolytic Solutions. *J. Electrochem. Soc.* **2008**, *155*, F13.

[70] Tsai, P.-C.; Wen, B.; Wolfman, M.; Choe, M.-J.; Pan, M. S.; Su, L.; Thornton, K.; Cabana, J.; Chiang, Y.-M. Single-particle measurements of electrochemical kinetics in NMC and NCA cathodes for Li-ion batteries. *Energy Environ. Sci.* **2018**, *11*, 860–871.

For Table of Contents Only